National Aeronautics and Space Administration

Measuring Azimuth Deformation with L-band Wide-Swath SAR Interferometry

Cunren Liang (329A) and Eric J. Fielding (329A)

1. Introduction

NISAR The upcoming NASA's NISAR mission carries an L-band wide-swath Synthetic Aperture Radar (SAR). L-band SAR interferometry can measure deformation with much lower noise level, while wide-swath has the benefit of imaging a large area and reducing revisit time.

Problem 1. Like regular SAR interferometry, wide-swath SAR interferometry also only measures Line-of-Sight (LOS) deformation on the ground. Azimuth (approximately north-south) deformation is critical for measuring 3-D deformation.

2. L-band SAR is more sensitive to ionosphere. Ionosphere causes azimuth shift in the azimuth deformation measurement. It should be corrected to improve the azimuth measurement accuracy.

Objective Our objective is to use an L-band wide-swath SAR to measure azimuth deformation and do ionosphere correction. We use L-band wide-swath SAR data acquired by JAXA's ALOS-2 mission to explore NISAR's potential of measuring large-area azimuth deformation.

2. Method

Azimuth Deformation ALOS-2 uses burst technique to acquire wide-swath image. A target on the ground can be imaged by several bursts. Each burst can measure the azimuth deformation projected onto its LOS (such as x_1). Azimuth deformation x can be calculated by combining two bursts.

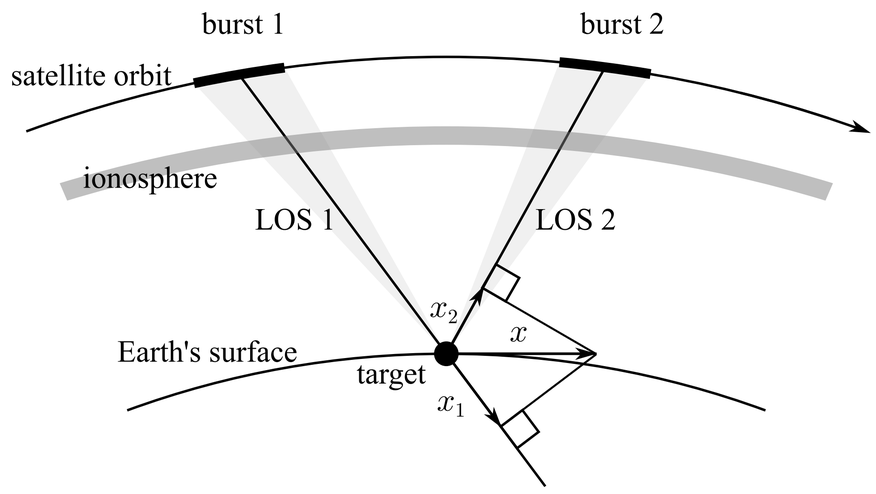

Ionosphere Correction The ionosphere shift in the azimuth deformation measurement can be calculated by

$$x_{ion,d} = \frac{v_g}{4\pi K_a}\frac{\partial \phi_{ion,d}}{\partial \eta}$$

where v_g is the velocity of the radar footprint on the ground, K_a is the azimuth frequency modulation rate, and η is the azimuth time.

Ionosphere phase delay $\phi_{ion,d}$ is inversely proportional to radar frequency. It can be estimated using a split-spectrum method.

This research is supported by NISAR Science Definition Team, NASA Earth Surface and Interior Project and NASA Postdoctoral Program. For more information, please see➔

National Aeronautics and Space Administration
Jet Propulsion Laboratory
California Institute of Technology
Pasadena, California

www.nasa.gov

- **C. Liang** and E. J. Fielding, "Interferometry with ALOS-2 full-aperture ScanSAR data," *IEEE Transactions on Geoscience and Remote Sensing*, vol. 55, no. 5, May 2017.
- **C. Liang** and E. J. Fielding, "Measuring azimuth deformation with L-band ALOS-2 ScanSAR interferometry," *IEEE Transactions on Geoscience and Remote Sensing*, vol. 55, no. 5, May 2017.
- I. J. Hamling, S. Hreinsdóttir, K. Clark, J. Elliott, **C. Liang**, E. Fielding et al., "Complex multi-fault rupture during the 2016 Mw 7.8 Kaikōura earthquake, New Zealand," *Science*, vol. 356, no. 6334, Apr. 2017. (**Cover Story**)

3. Result

2015 Mw7.8 Nepal Earthquake The azimuth deformation is very different from the LOS deformation measured by regular SAR interferometry. The maximum azimuth deformation caused by this earthquake is up to 2.6 m.

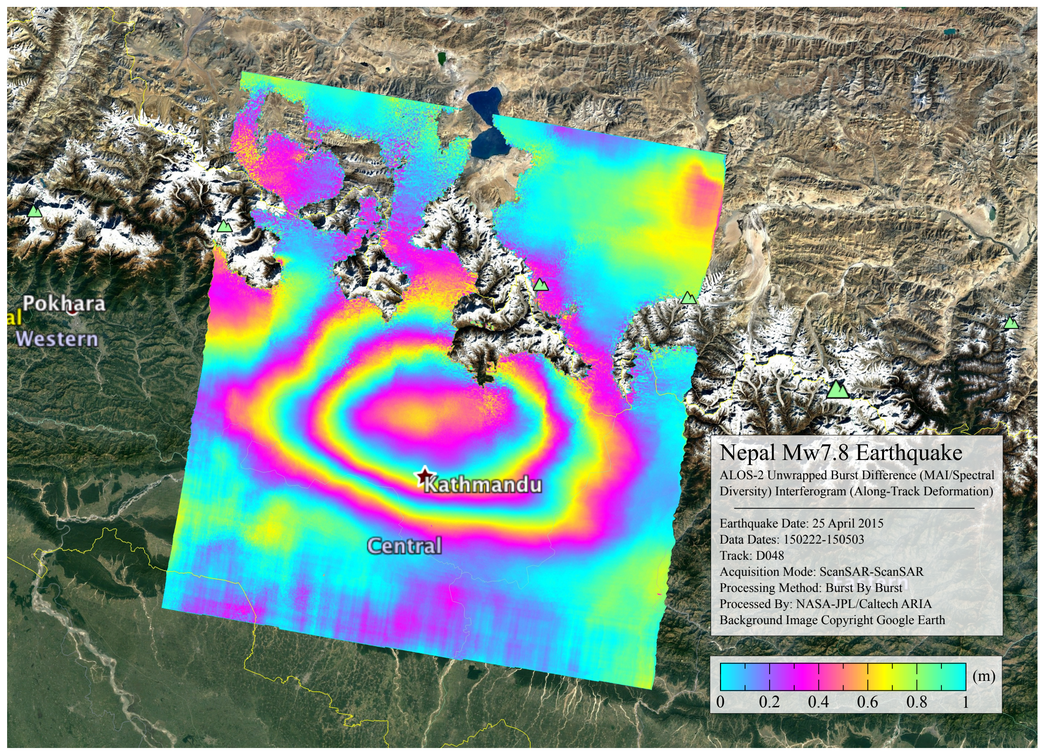

2016 Mw7.8 New Zealand Earthquake From azimuth deformation map, a number of known and unknown faults can be identified, which is important to the study of this very complex earthquake.

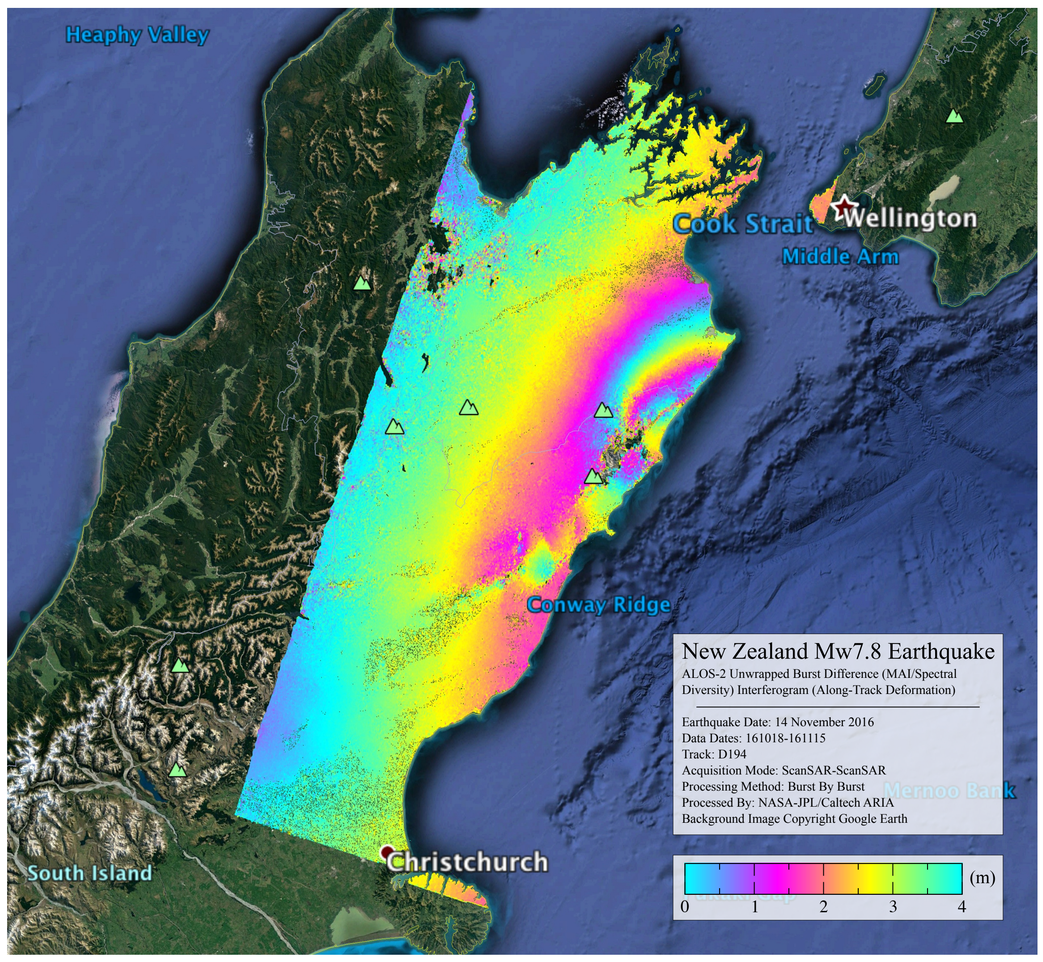

4. Conclusion

- For the first time, azimuth deformation of a large earthquake is completely measured by L-band wide-swath SAR interferometry.
- Results have already contributed to earthquake research (Hamling et al., 2017, Science).
- With SweepSAR technology and an extra range band, NISAR should be able to achieve much better accuracy than ALOS-2.

Poster No. EA-01

National Aeronautics and Space Administration

Utilizing a suite of NASA satellite missions for analysis of the Aral Sea desiccation

Author: Alka Singh(329E)
Advisor: Ali Beharangi (329E)

Introduction

Closing the water balance in most of the region is exceedingly difficult due to the sparsity of field observation, large uncertainties in satellite derived estimates and model limitation. The study integrated multiple NASA satellite missions in order to compute total water storage (TWS) of the Aral Sea and its basin and analyzed the Aral Sea desiccation.

Objective

- Evaporation estimation from the Aral Sea water body
- Runoff estimation into the selected sub basin

Study area

The Aral Sea has become a major ecological disaster during the 20th century, due to largescale irrigation abstraction from its two primary inflow Amu Darya and Syr Darya. The Figure-1 shows the major canal irrigation region of the Aral Sea basin. The yellow region in the Figure-1 shows the analyzed Aral Sea sub-basin, demarcated based on the GRACE gravity field missions mascon grid.

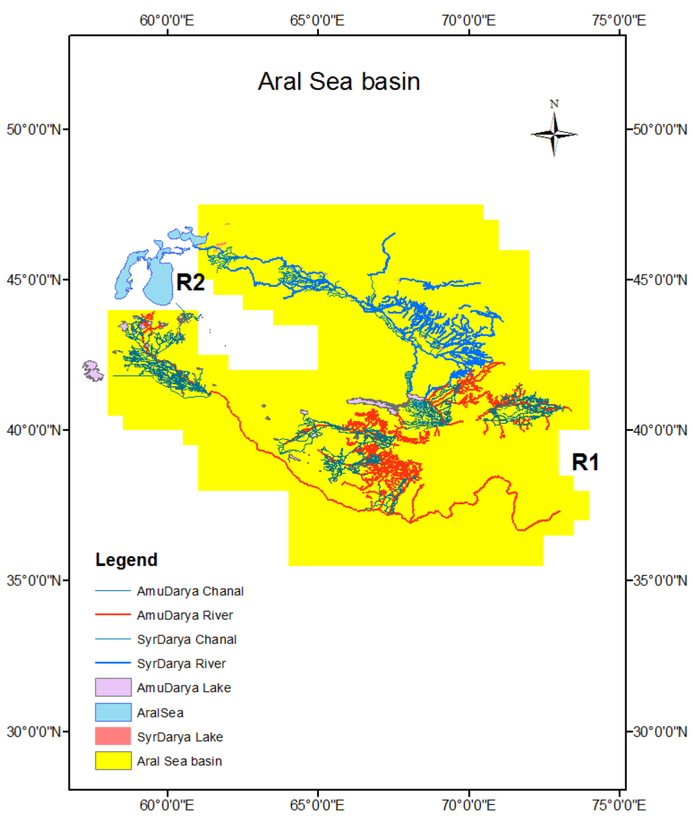

Figure 1: Study area. R1 is the derived total drainage from the Amu Darya and the Syr Darya into the selected Aral Sea sub-basin (yellow region) and R2 is the total drainage into the Aral Sea waterbody obtained from in-situ observations.

Method

- The Aral Sea water volume is estimated at a monthly time steps by a combination of the Landsat and altimetry (Jason 1 and Jason 2) observations, using truncated pyramid method.
- Monthly differential of the lake volume variation is used as an constrain to the integrated hydrological fluxes acting on the lake, in order to estimate evaporation.

$$E = P + R2 - \partial\, lake\, volume$$

- Further, the study is extended to the irrigated belt of the Aral Sea basin to evaluate the impact on runoff. At a sub basin level, the derivative of GRACE based TWS (∂G) is used as an constrain to estimate a runoff into the basin (R1) from the other hydrological fluxes.
  - $R1 = \partial G\text{-}(P\text{-}ET\text{-}R2)$
- In order to assess the uncertainties in the input fluxes precipitation data from TRMM, GPCC, ERA and GPCC and evaporation estimations from GLDAS, WGHM and MOD16 has been analyzed.

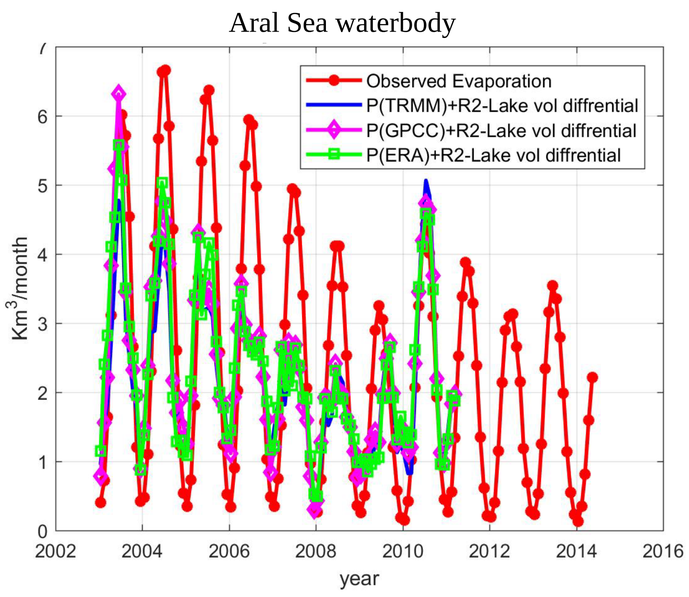

Figure 2: The Aral Sea waterbody: MODIS based potential evaporation is compared with the evaporation estimates back calculated from the TWS of the lake

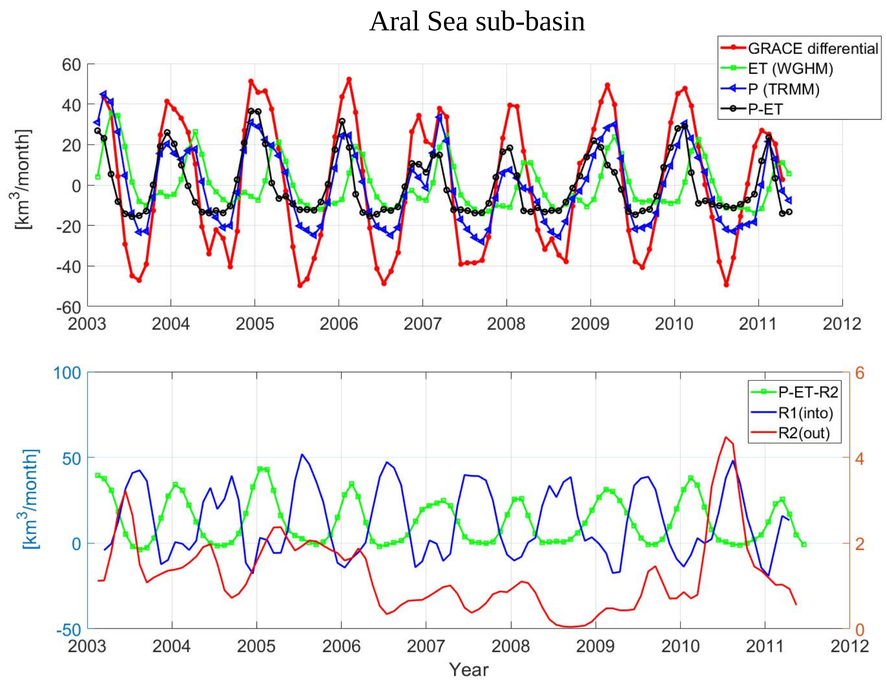

Figure 3: The Aral Sea sub-basin: R1 estimation from the GRACE based TWS and the other hydrological fluxes (for e.g. ET from WGHM and P from TRMM)

Results

- The Aral Sea water body volumetric variation has 90% correlation with the net hydrological fluxes. All precipitation datasets (TRMM, GPCP, GPCC, ERA) have very high correlation.
- The estimated E from the TWS and MODIS showed good long-term agreement (77% correlation). However, summer peaks are over estimated by the MODIS based potential evaporation of the waterbody.
- At a sub-basin level P-ET has 82% correlation with the ∂G, which shows that major mass loss trend observed by GRACE came from P-ET.

Summary

- The TWS of the lake is computed by altimetry based water height and high resolution Landsat data. The lake TWS is constrained by in-situ runoff to compute E estimate.
- The figure-2 indicates that ET is the most uncertain parameter in this region and can be back calculated from the TWS. P has limited contribution over the lake.
- The runoff estimation method showed in figure-3 can be used to estimate long term variations in runoff.

Acknowledgement

The authors acknowledge the financial support made available by NASA GRACE and GRACE-FO (NNH15ZDA001N-GRACE) and NASA Energy and Water Cycle Study (NNH13ZDA001N-NEWS) awards. Special thanks to Joshua Fisher (329G) and Halverson Gregory (329G) from JPL for providing MODIS based potential evaporation and actual evapotranspiration estimates

National Aeronautics and Space Administration

Jet Propulsion Laboratory
California Institute of Technology
Pasadena, California

National Aeronautics and Space Administration

Using NASA Satellite Observations to Map Wildfire Risk in the United States

Author: Alireza Farahmand (329E)
JT Reager (329F), Ali Behrangi (329E), Natasha Stavros (398P), James Randerson[1]
[1] University of California, Irvine

Introduction

Fires are a key disturbance globally acting as a catalyst for terrestrial ecosystem change and contributing significantly to both carbon emissions and changes in surface albedo. The socioeconomic impacts of wildfire activities are also significant with wildfire activity results in billions of dollars of losses every year. Numerous studies have aimed to predict the likelihood of fire danger, but few studies use remote sensing data to map fire danger at scales commensurate with regional management decisions (e.g., deployment of resources nationally throughout fire season with seasonal and monthly prediction). Here, we use NASA Gravity Recovery And Climate Experiment (GRACE) assimilated surface soil moisture, NASA Atmospheric Infrared Sounder (AIRS) vapor pressure deficit, and landcover products, along with US Forest Service historical fire activity data to generate probabilistic monthly fire potential maps in the United States. These maps can be useful in not only government operational allocation of fire management resources, but also improving understanding of the Earth System and how it is changing in order to refine predictions of fire extremes.

Datasets

- Pre-season Jan-Apr GRACE-assimilated Soil Moisture
- 1-month lead AIRS Vapor Pressure Deficit (VPD)
- Monthly fire counts from USDA Forest Service's Fire Program Analysis Fire-occurance database (FPA FOD)
- USGS National land-cover databse

Methodology

- First, we develop a 2-D space of SM and VPD values for all land cover types deciduous, evergreen, shrub land, herbaceous, and wetland. The space splits each variable into 20 equal-sized ranges. For each bin in the space , we then calculate:

$$p(fire) = \frac{toral\ fire\ occurances}{total\ sm\ VPD\ combinations}$$

One look-up table is generated for each land-cover type and each month. Once a real-time SM ad VPD observation becomes available, the corresponding look-up table will be utilized to predict the likelihood of fire occurrence. Figure 1 shows look-up tables generated using Jan-Apr SM and July VPD observations for predicting the likelihood of fire occurrence in August.

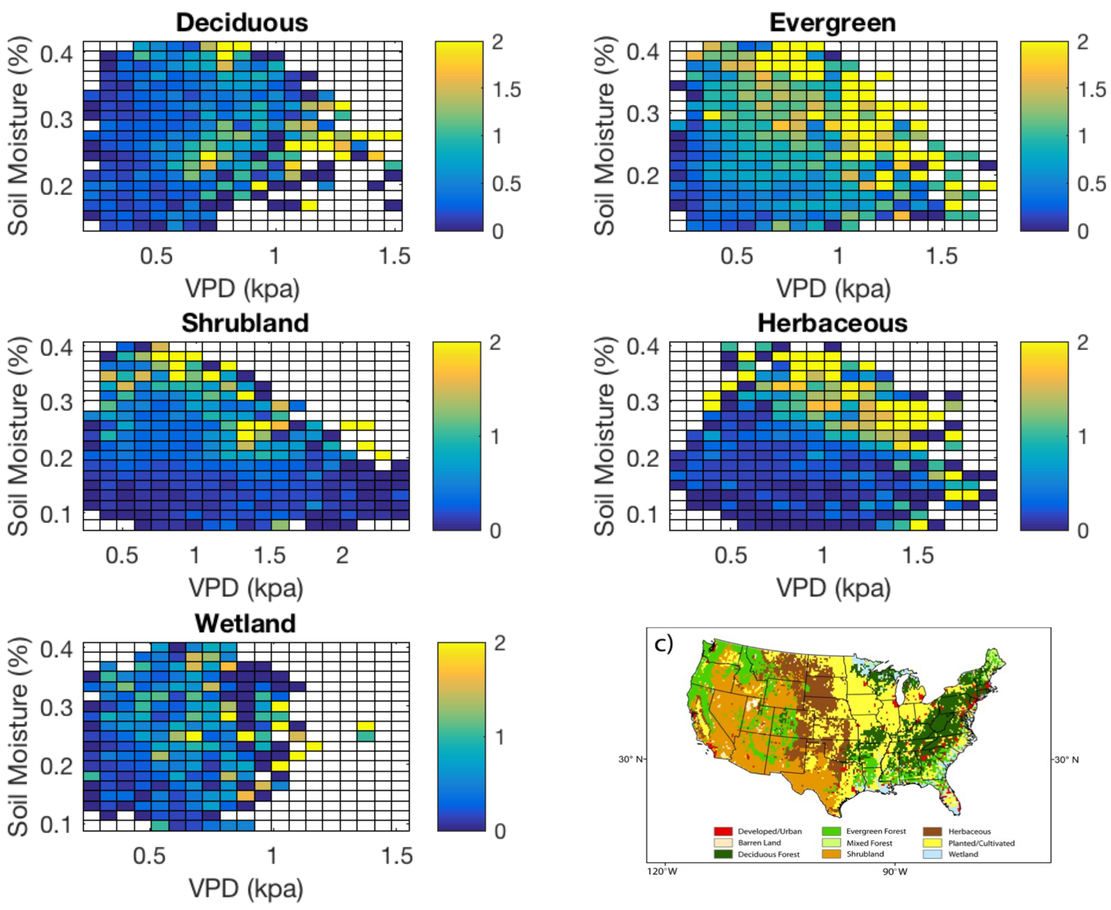

Results

Figure 2 shows Jan-Apr 2012 SM and July 2012 VPD observations, observed number of fire occurrences and predicted likelihood of fire occurrence for August 2012. The first row shows Jan-Apr 2012 Soil Moisture and July 2012 VPD observations. The second row shows the observed and predicted likelihood of fire occurrences for August 2012. As shown , observed and predicted maps show consistent patterns in the entire United States.

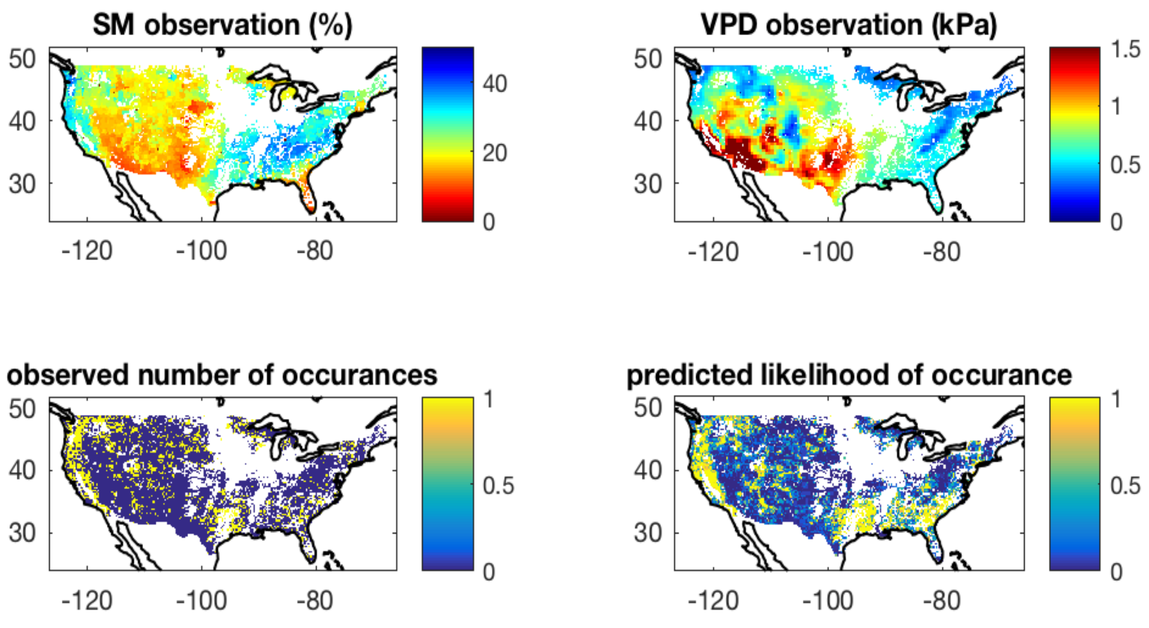

Figure 3 shows the validation of the model framework across different landcover and GACC types. Figure 3a shows GACC types across the US. Figure 3b shows the time series of monthly average fire observations and simulations in GACC Eastern. Figure 3c shows the total number of fire observations and simulations across various landcover types. Figure 4d shows the spatial map of RMSE between simulations and observations.

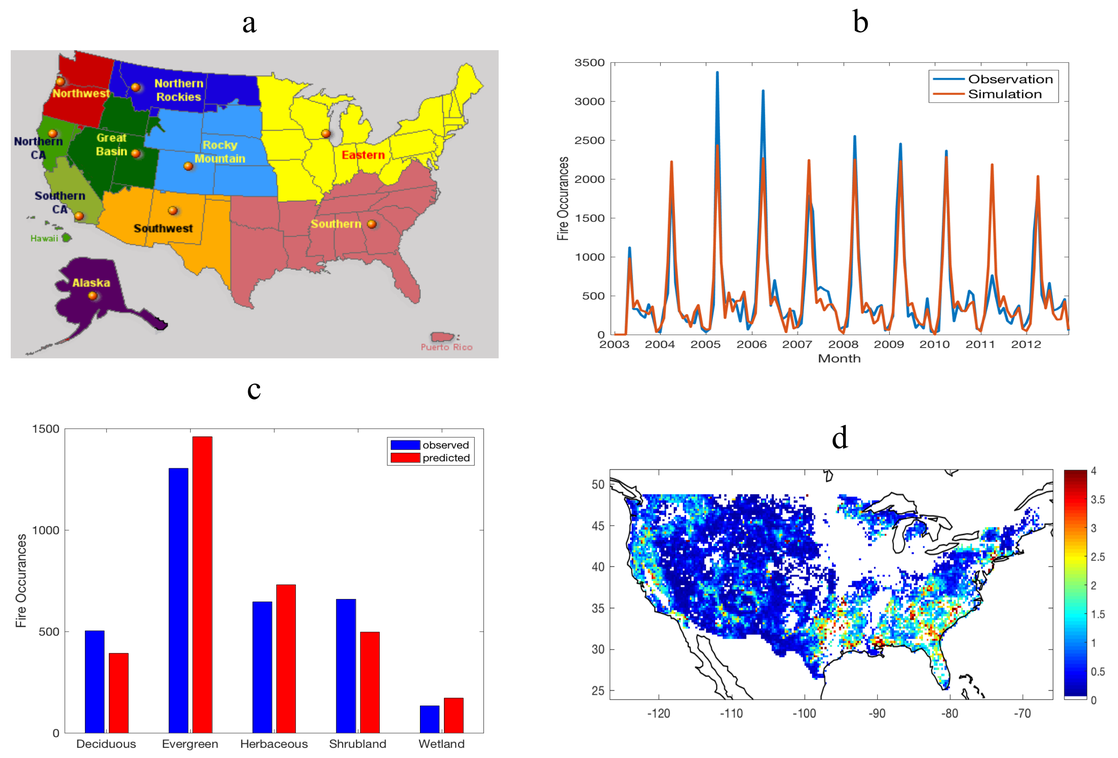

Conclusion

- This study used January through April Soil Moisture and 1-month leading time VPD data to predict the likelihood of monthly fire occurrences.
- We have validated the model across various landcover and GACC types. The result show that the model can potentially predict the likelihood of fire occurrences with relatively small margin of errors.
- These maps can be useful in not only government operational allocation of fire management resources, but also improving understanding of the Earth System and how it is changing in order to refine predictions of fire extremes
- The future work includes investigating other hydrologic variables including vegetation greenness and precipitation data to improve the model performance.

National Aeronautics and Space Administration
Jet Propulsion Laboratory
California Institute of Technology
Pasadena, California

www.nasa.gov

Poster No. EA-04

National Aeronautics and Space Administration

Combining Remote Sensing Data, Airborne Snow Observations and High Resolution Hydrologic Modeling to Improve SWE Estimates over Western US Mountainous Terrain

Author: Catalina M. Oaida (329)

Co-Authors: John T. Reager (329), Kostas Andreadis (329), Steve Levoe (398), James Famiglietti (329)

I. Introduction

- The mountain snowpack is an important component of the hydrologic cycle and an essential **water resource** for communities across the globe.
- Being able to correctly estimate **snow** is not only a great necessity for scientists, water resource managers and decision makers, but also a challenge.
- **Western States Water Mission** (JPL):
  - Goal: provide accurate and accessible water availability data products for the U.S. western states to water applications stakeholders and the scientific community through a convenient user interface.
  - **Leverage space and air-borne NASA data products in conjunction with hydrologic models to improve water availability estimation.**
- **Estimating snow** amount is a crucial component of achieving these goals

II. Objective

- Improve snow water equivalent (SWE) estimation over the Western U.S. (WUS) using data assimilation (DA) of space-borne data and high-resolution hydrologic modeling.
- Evaluate against spatially distributed Airborne Snow Observatory (ASO) data.

Challenge

- Assimilating *snow cover* (SC) observations to update *SWE* estimates.
- Instantaneous SC does not provide that much information on instantaneous SWE

III. Methodology

- *Batch smoother* method desirable for snow DA, considers evolution of SC throughout the season to inform SWE updates (vs sequential filter method).
- Compare "assimilation" and "no assimilation" cases against observations to assess improvement.
- Goal of work shown here: evaluate this method on smaller river basins (where ASO available) then expand and use method on larger area (WUS).

Domain: Tuolumne River Basin, CA

Spatial resolution: 1.75 km x 1.75 km (~ 3 km^2)

Temporal coverage: WY 2013-2016, daily time step (snow model, 3h step)

DA: Local Ensemble Transform Kalman Filter. To avoid spurious correlations during early accumulation season, assimilation window limited to Jan-Jul.

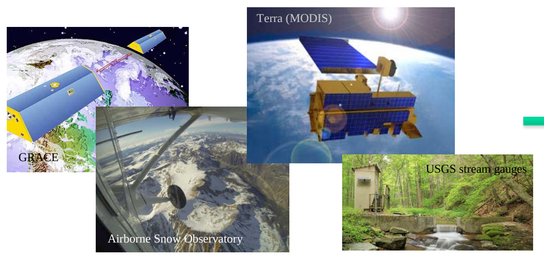

1. Observations

WSWM

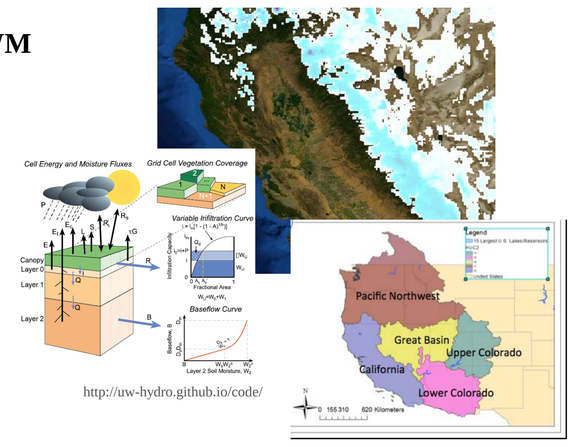

http://uw-hydro.github.io/code/

2. High Resolution Modeling

3. Estimates with uncertainties

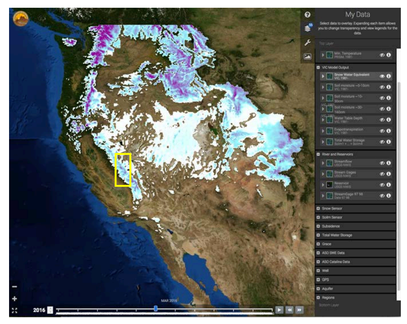

4. Interactive data analytics

5. USERS
Stakeholders
Water resource managers
Policy makers
Scientists

Full WSWM domain & Tuolumne RB domain in this study

Data:

Assimilation: **MODSCAG** (MODIS Snow Covered Area and Grain Size) - daily snow cover fraction; native resolution: 500 m

Validation: **ASO** (Airborne Snow Observatory) SWE; select dates during spring season; native resolution: 50 m

Models:

VIC (Variable Infiltration Capacity, *U. Washington, Liang et al. (1994)*) semi-distributed macro-scale hydrologic model

RHEAS software (JPL, *K. Andreadis*) – snow DA (based on Hunt et al. (2007)):

- Calculates SWE and SC climatology once (here, 1981-2010)
- Random sampling of climatology to construct background ensemble
- Computes optimal weights between SC background state and SC observations given model and observations errors (background perturbation errors and obs errors)
- Weights used to updates SWE state variable

Finding the appropriate DA implementation

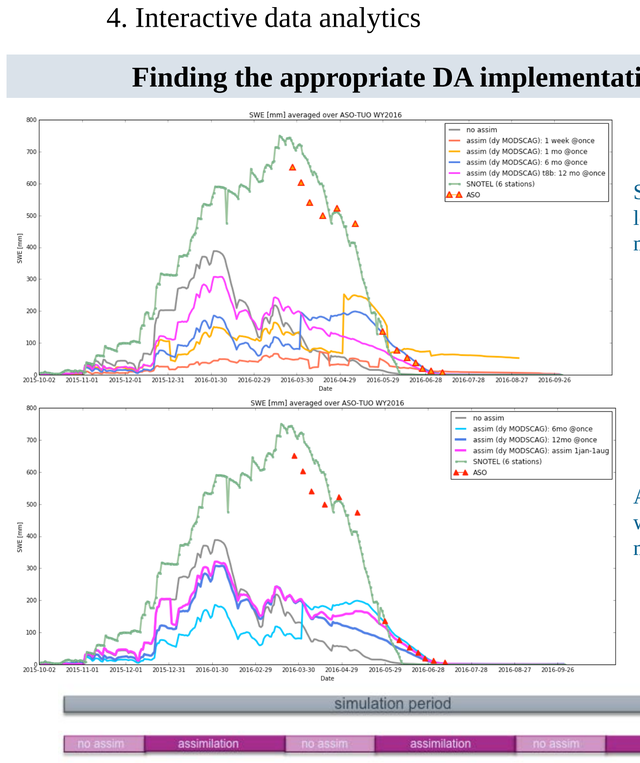

Simulation length matters

Assimilation window matters

Fig 1. SWE [mm] time series for WY 2016; assimilation window sensitivity studies. Bottom: schematic showing temporal implementation of assimilation method.

IV. Results

→ Model captures SWE **temporal variability** well: good temporal correlations vs in-situ (SNOTEL) data

→ Model underestimates peak SWE in average and wet years.

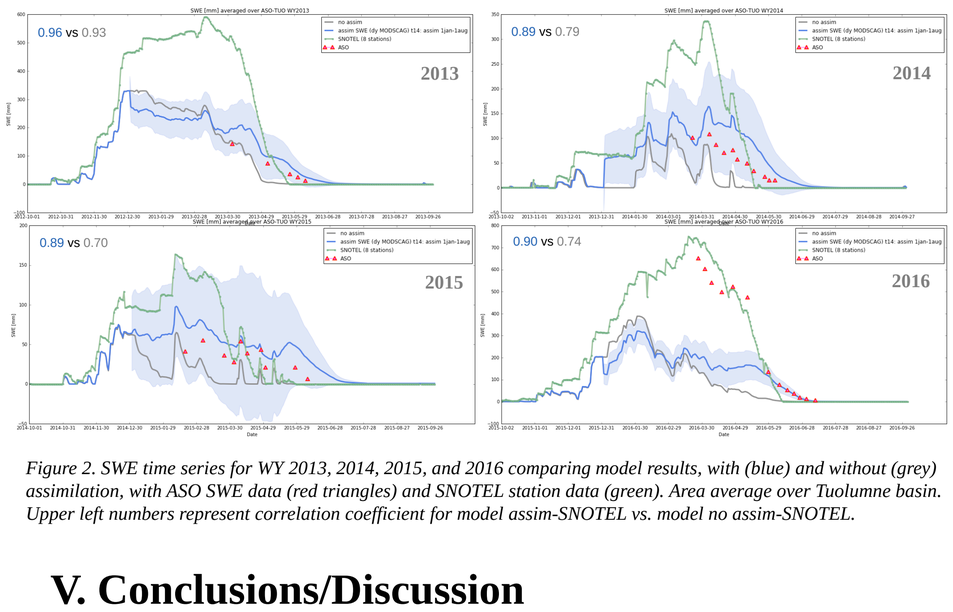

Figure 2. SWE time series for WY 2013, 2014, 2015, and 2016 comparing model results, with (blue) and without (grey) assimilation, with ASO SWE data (red triangles) and SNOTEL station data (green). Area average over Tuolumne basin. Upper left numbers represent correlation coefficient for model assim-SNOTEL vs. model no assim-SNOTEL.

→ Assimilation improves SWE **spatial distribution** wrt ASO

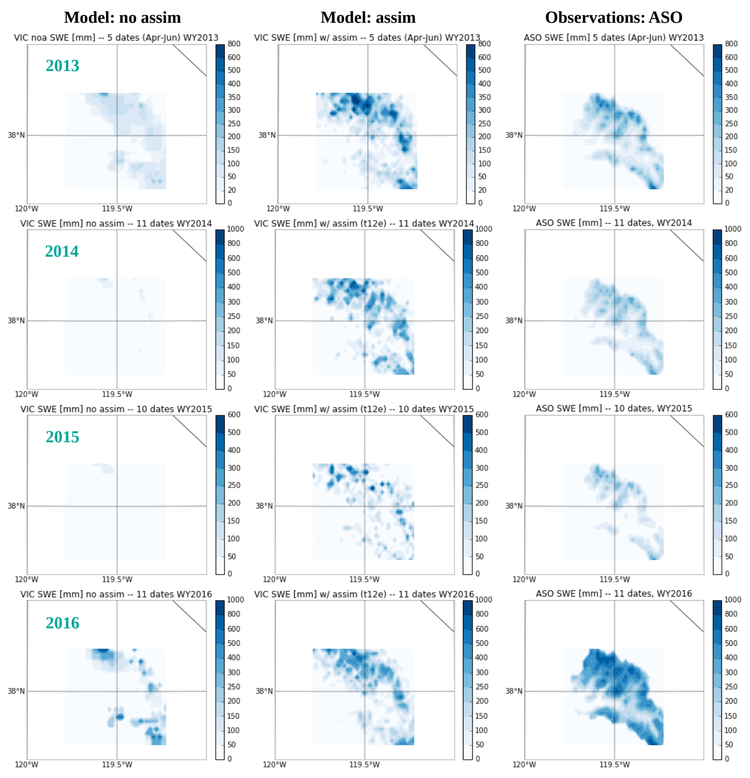

Figure 3. SWE [mm] spatial maps, averaged over select spring dates when ASO is available: model no assimilation (left), model with MODSCAG assimilation (center), and ASO (right). ASO data (50 m) regridded/aggregated to VIC spatial resolution (1.75 km).

→ In assimilation case:

- More SWE throughout all elevation bands
- In dry years, deeper snowpack, and more snow at mid & high elevations
- In average year, SWE distributed more evenly across elevation bands instead of clustered at high elevations

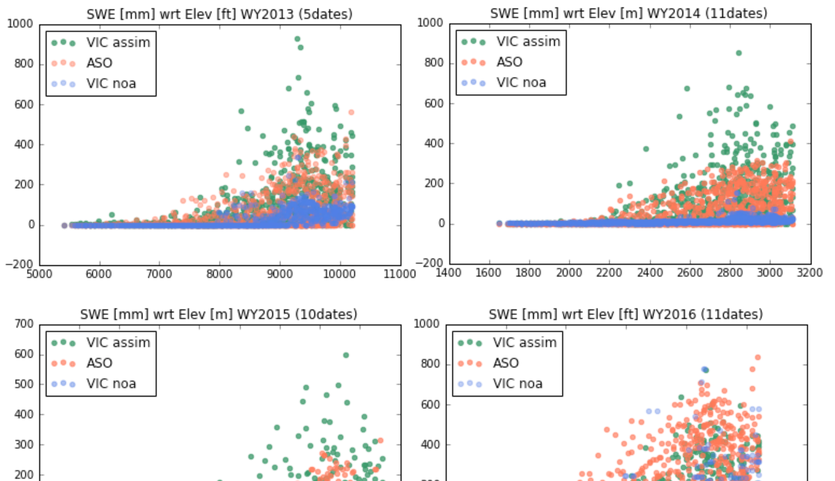

Figure 4. SWE [mm] with respect to elevation. Model data selected for ASO dates only.

V. Conclusions/Discussion

- New method (Local Ensemble Transform Kalman Filter, LETKF) tested for snow DA
  - Benefit of this LETKF: its **relative simplicity**, **ease of implementation** & **computational efficiency** (parallelization, 1-time climatology)
  - Assessed over smaller area, but can be easily scaled up to larger domain
- Validate DA method against ASO SWE product: new-most studies evaluate against station (snow pillows) data, which don't capture spatial distribution and variability.
- Assimilation improves SWE estimates over open-loop (no assim) case when compared with observations, both **temporally** and **spatially.**
  - Model preforms better during drier years (vs average years), and during the melting season (vs accumulation).

- Model underestimates peak SWE during average snow years (e.g. WY2016) but performs well during drier (drought) years.
  - Underestimation of peak SWE likely due to model parameterization - inadequate, simplistic snow depletion curve (SDC).
- Assimilating *SC* to updated *SWE* remains a challenge, especially when near-real time updates are desirable (vs reanalysis methods)
- WSWM successfully (i) developed framework and (ii) tested new snow DA for multi-year period (17 years) over large area (western US) at high resolution (3 km^2), overcoming computational challenges associated with such task.

National Aeronautics and Space Administration

Jet Propulsion Laboratory
California Institute of Technology
Pasadena, California

www.nasa.gov

Poster No. EA-06

Characterizing the Diurnal Cycle of Land Surface Temperature and Evapotranspiration using Thermal Observations from Small UAVs

National Aeronautics and Space Administration

Debsunder Dutta (329G-Caltech)
Darren Drewry (329G), William Johnson (389N) and Roland Brockers (347H)

1. Introduction

1. Small UAVs with lightweight sensors offer the potential to capture the diurnal variability in Land Surface Temperature (LST) at high spatial resolutions.
2. Commercial low-cost sensors (e.g. Tetracam + FLIR Tau- 2 module) are capable of acquiring co-registered multispectral (Vis-NIR) and thermal imagery from UAVs.
3. However the spotmeter based temperature measurements from these uncooled microbolometer based FPA sensors are unstable and inaccurate.

2. Objectives

1. Develop ambient operating temperature dependent calibrations for retrieving LST without the use of spotmeter for long term field deployment for monitoring vegetation.
2. Incorporate LST measurements and flux tower observations into physically based energy balance frameworks for characterizing the diurnal cycle of evapotranspiration (ET) over agricultural systems.

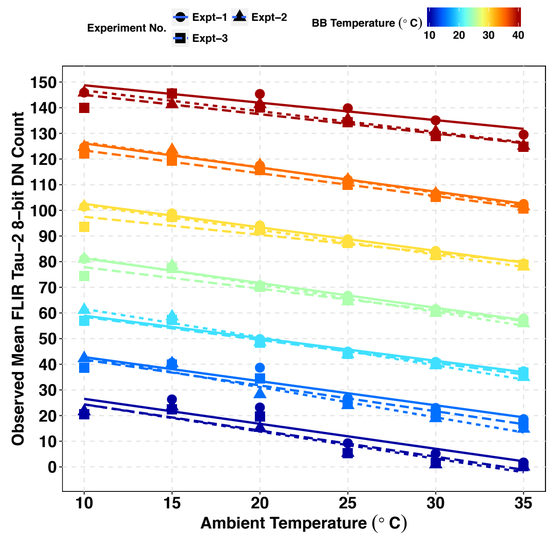

Fig. 1. JPL thermal chamber experimental results showing a consistent pattern of ambient -temperature dependent instability across a range of blackbody temperatures.

3. Calibration

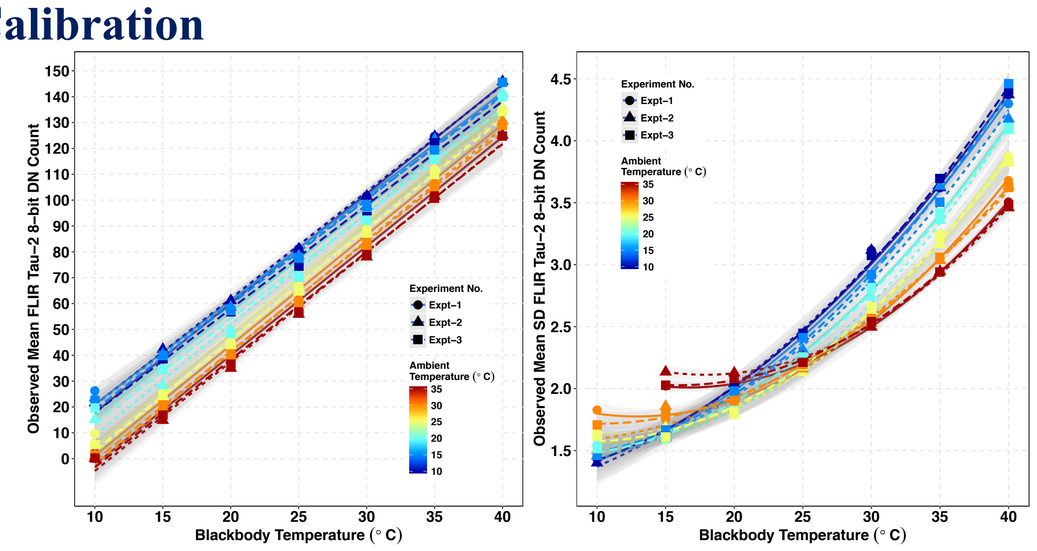

*Fig.2 **(Left)** Experimental results showing the relationship (calibration) between the mean FPA DN counts and blackbody temperatures for a range of ambient sensor temperatures. **(Right)** Results showing the non-linear relationships between the mean standard deviation (uncertainty) of FPA DN counts and blackbody temperatures for a range of ambient sensor temperatures.*

1. FPA-Temperature = Mean Calibration + FPA Non-uniformity correction *(each term = f(amb temp))*
2. Maximum value of ambient temperature dependent FPA NUC ~ ± 1℃.
3. Independent validation show error in pixel wise temperature prediction from calibration is ± 1℃.

4. Field Campaign – Russell Ranch

1. Data acquisition at Russell Ranch, Davis, CA on 27th April 2017 - capturing diurnal variability in LST.
2. Tetracam sensor (6band VNIR + FLIR Tau-2 thermal channel).
3. UAV flights over targets (metal plates and tarps) and crop validation plots to capture the diurnal variability in LST.
4. Laboratory derived mean and FPA non-uniformity calibrations are applied to the thermal imagery.
5. Imagery is orthorectified and mosaicked together.
6. Imagery represents the warming and cooling trends of the target and crops well.

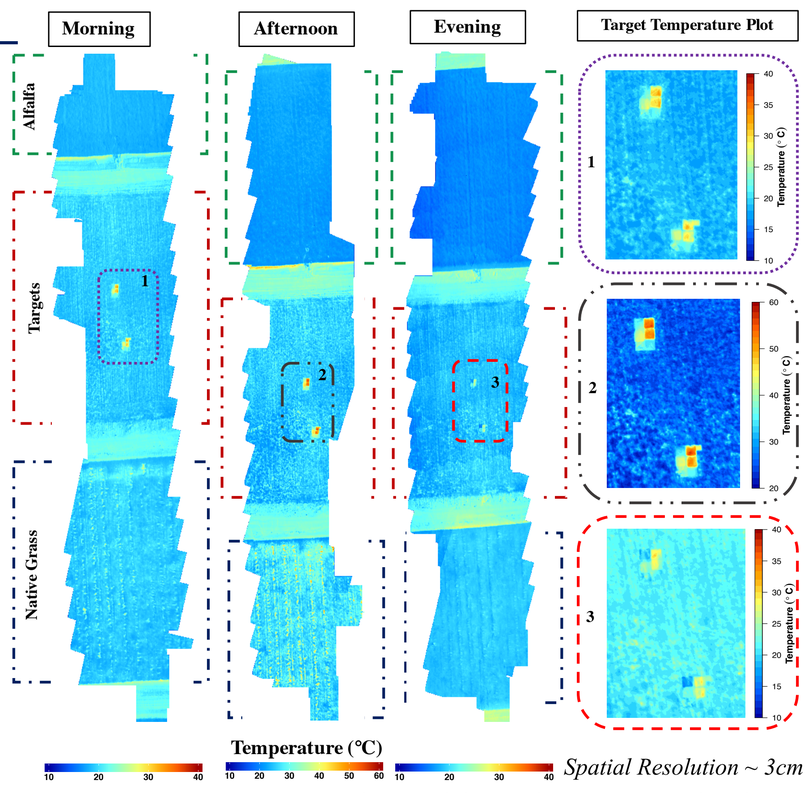

Fig.3 N-S transects over target and crop validation plots at RR agricultural sites in Davis, CA. The acquisition times are 9:30am (morning), 12:00 pm (afternoon) and 6:15 pm (evening).

5. Results –Validation and Diurnal Trends in LST

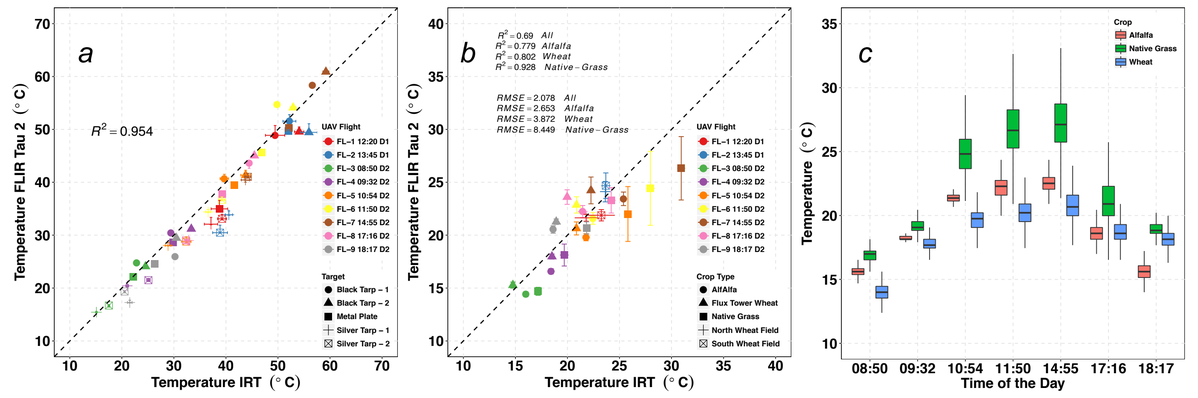

*Fig. 4 Scatterplots representing the UAV measured target temperatures (**panel-a**) and crop temperatures (**panel-b**) versus corresponding IRT ground measurements for 9 flights spanning the April, 26 (D1) and 27 (D2) , 2017. The errorbars represent the one standard deviation uncertainty along both x and y axes. **Panel-c** boxplots showing the diurnal variation in the spatial distribution of crop temperatures as measured from UAV acquisitions for April 27, 2017.*

6. Computing Evapotranspiration

1. The Surface Temperature Initiated Closure (STIC) model is used for computing ET Fluxes.
2. STIC provides a physically based surface energy balance framework for simultaneous retrieval of the surface and atmospheric conductance and surface energy fluxes (latent and sensible heat) by physically integrating radiometric surface temperature into the Penman-Monteith equation.

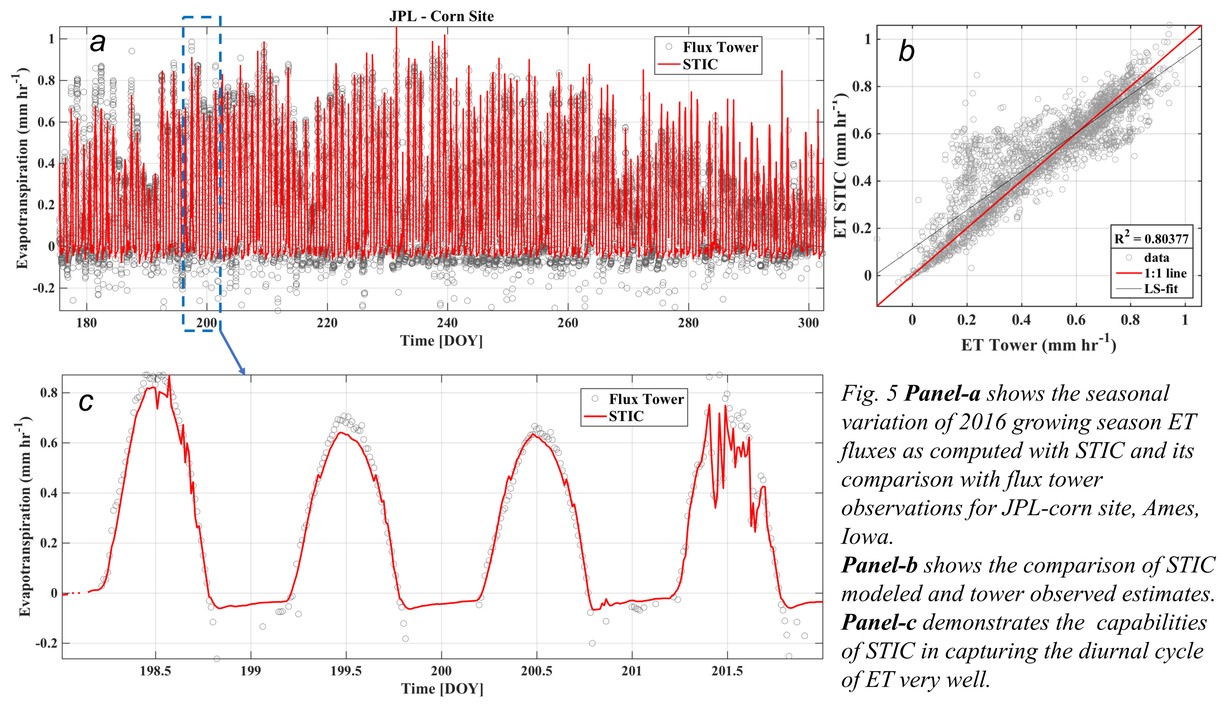

*Fig. 5 **Panel-a** shows the seasonal variation of 2016 growing season ET fluxes as computed with STIC and its comparison with flux tower observations for JPL-corn site, Ames, Iowa.*
***Panel-b** shows the comparison of STIC modeled and tower observed estimates.*
***Panel-c** demonstrates the capabilities of STIC in capturing the diurnal cycle of ET very well.*

7. Spatial and Diurnal Variation in ET

Fig. 6 Results of ET computation from data collected at Sweeney Corn site in Ames, Iowa.
***Panel-a** shows the NDVI computed using the 850nm and 650nm channels of the Tetracam.*
***Panel-b** shows the derived LST using the 11000 nm (center wavelength) co-registered FLIR Tau-2 channel and **Panel –c** shows the ET computed using LST and flux tower observations on site. The imagery was collected on August 6, 2016 at 11:30 am local time.*
The spatial structure of the corn rows are clearly observed as well as the distinction between grassy areas and corn.
***Panel-d** shows the diurnal variability in ET captured from UAV with the STIC modeled and flux-tower observed values for August 6, 2016.*

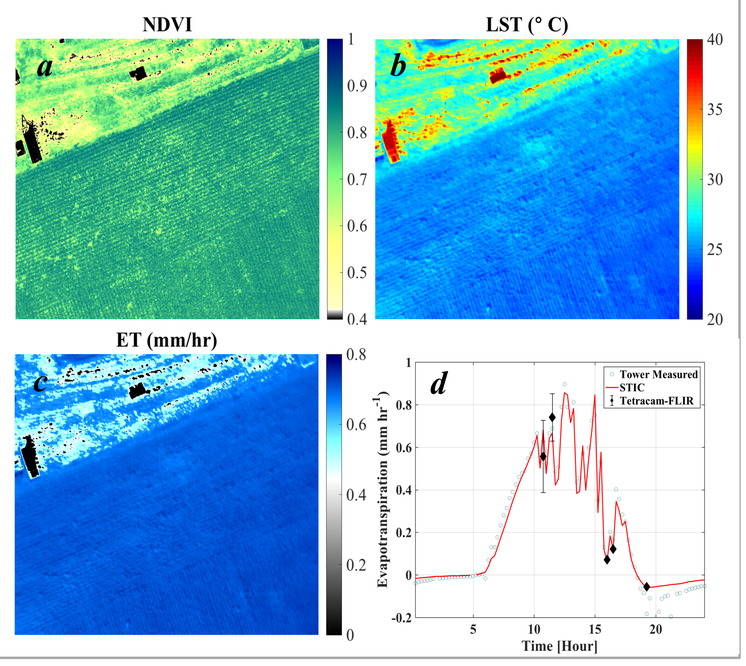

8. Conclusions

1. The developed calibration methodology allows accurate retrieval of LST using low cost microbolometer sensors from sUAV platforms with an error ± 1℃.
2. We demonstrate the applicability of STIC for computing ET from radiometric LST observations and capturing the diurnal variability of ET.
3. This methodology using sUAS could be used for validating the diurnal cycle of ET and LST from ECOSTRESS mission in future.

National Aeronautics and Space Administration

Jet Propulsion Laboratory
California Institute of Technology
Pasadena, California

www.nasa.gov

Poster No. EA-07

National Aeronautics and Space Administration

How does your terrestrial model stack up in the Arctic-Boreal Region?

Author: Eric Stofferahn (329G-Caltech)
Co-Authors: Joshua Fisher (329G), Daniel Hayes (U. Maine), Deborah Huntzinger (Northern Arizona), Christopher Schwalm (Woods Hole), Wouter Hantson (U. Maine)

Motivation

Address Key ABoVE Indicators

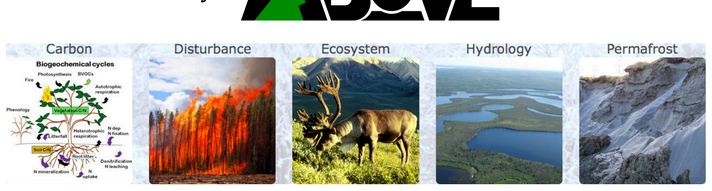

- How are the magnitudes, fates, and land-atmosphere exchanges of carbon pools responding to environmental change, and what are the biogeochemical mechanisms driving these changes?
- What processes are contributing to changes in disturbance regimes and what are the impacts of these changes?
- How are flora and fauna responding to changes in biotic and abiotic conditions, and what are the impacts on ecosystem structure and function?
- What are the causes and consequences of changes in the hydrologic system, specifically the amount, temporal distribution, and discharge of surface and subsurface water?
- What processes are controlling changes in the distribution and properties of permafrost and what are the impacts of these changes?

Benchmarking System

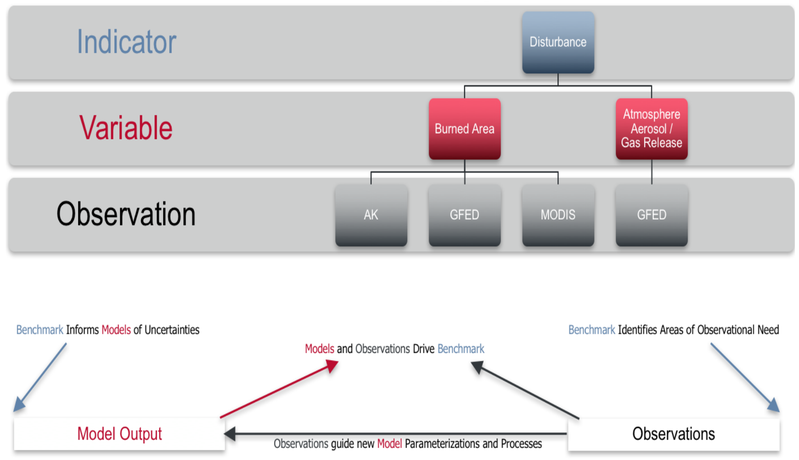

The benchmarking system is based upon ILAMB and will eventually be incorporated into ILAMB. The system will reside on the ABoVE Science Cloud, enabling fast access to current and future ABoVE data as well as other datasets relevant to the ABoVE region.

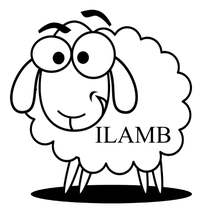

Datasets

Examples of dataset observation sources

Process

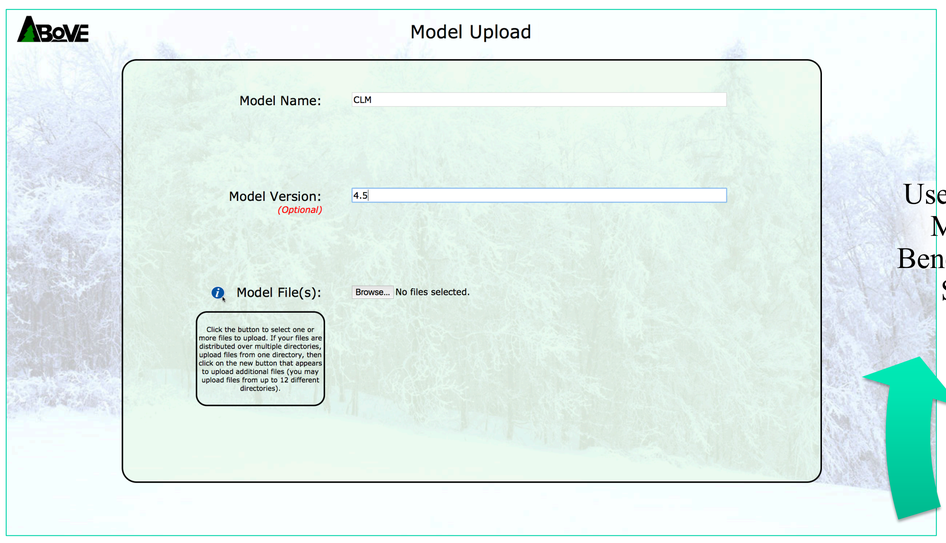

User Uploads Model to Benchmarking System

Benchmarking System Calculates Scores, Makes Graphics, and Builds Custom Webpage

User Views Results on Custom Webpage

User Updates Model Based on Benchmark Results

Version 1.0 → Version 1.5 → Version 2.0

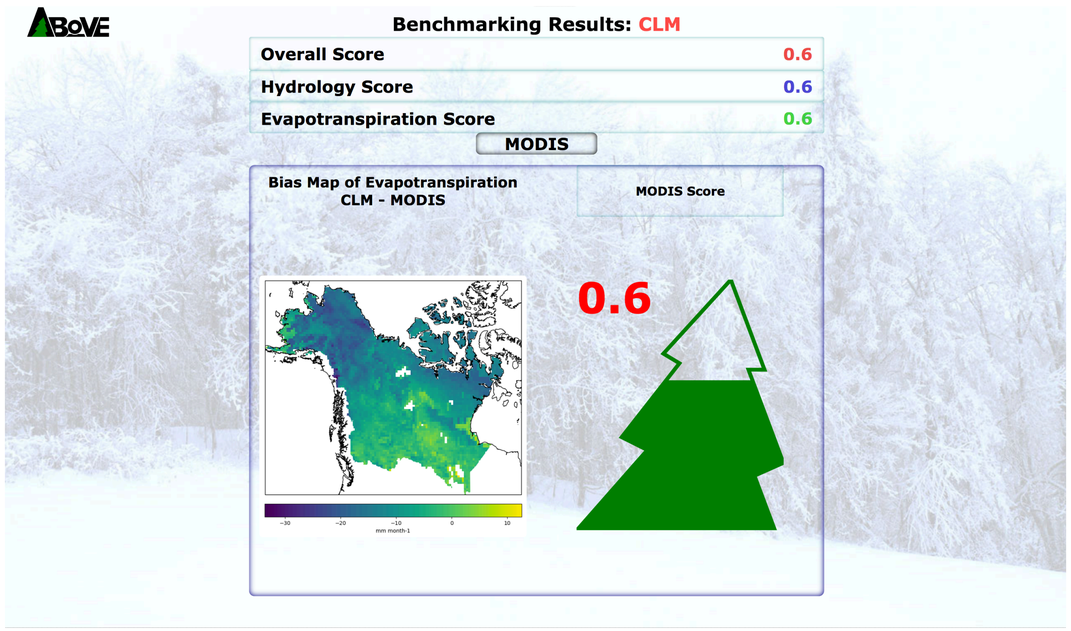

Functional Benchmarks

The benchmarking system will utilize functional benchmarks to explore the relationship of a given variable on one or more driver variables. This allows modelers to determine if their model is accurately representing the inter-dependence of these key Arctic processes.

National Aeronautics and Space Administration
Jet Propulsion Laboratory
California Institute of Technology
Pasadena, California

www.nasa.gov

Author Affiliations:
- California Institute of Technology
- University of Maine
- Northern Arizona University
- Woods Hole Research Center

Poster No.
EA-09

National Aeronautics and Space Administration

Scaling solar-induced fluorescence (SIF) from the leaf to the satellite

Author: Troy Magney (329G)

Christian Frankenberg (Caltech), Philipp Koehler (Caltech), Ying Sun (Cornell), Katja Grossman (UCLA), Jochen Stutz (UCLA), Joshua Fisher (329G)

Introduction:

- Recent advances have been made in the retrieval of solar-induced **chlorophyll fluorescence (SIF)** from space and could provide a **significant step towards mapping instantaneous plant photosynthesis across space and time**.
- While these advances are promising, there are still many **unresolved issues** related to the spatial, spectral, and temporal scale-change problem, making **interpretation of the mechanisms driving the SIF signal** from space challenging.

Global SIF as a proxy for photosynthesis?

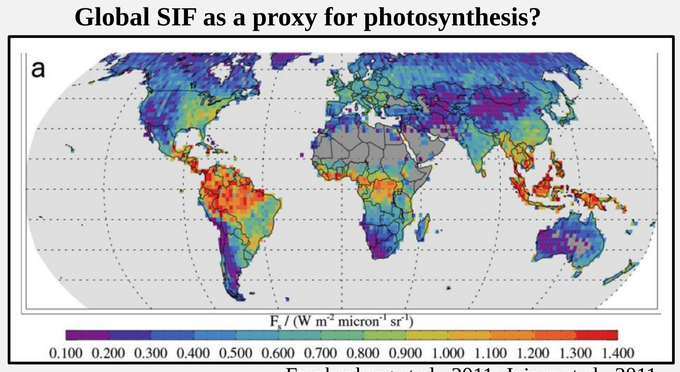

Frankenberg et al., 2011; Joiner et al., 2011

Primary Objectives:

- Leaf – changes in spectral shape of SIF signal
- Tower – diurnal and seasonal changes in SIF signal
- Airborne – spatial changes in SIF signal
- Satellite – improved interpretation of SIF signal

Leaf approach:

- Measure photosynthesis, active, and passive fluorescence simultaneously.
- Over a range of physiological conditions, species, and environments.
- Analyze changes in spectral shape coincident with changes in physiological function.

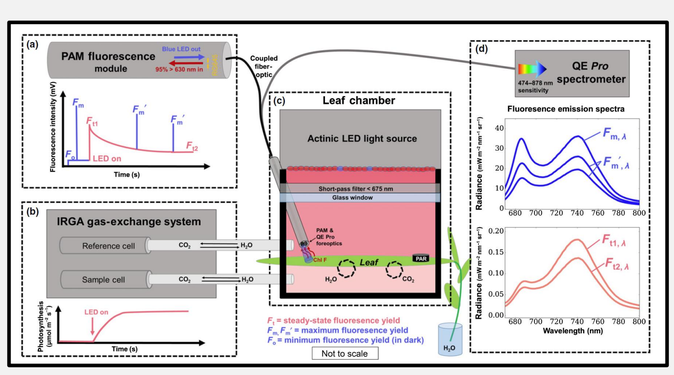

Schematic of gas-exchange, active/passive fluorescence system: Magney *et al.*, 2017

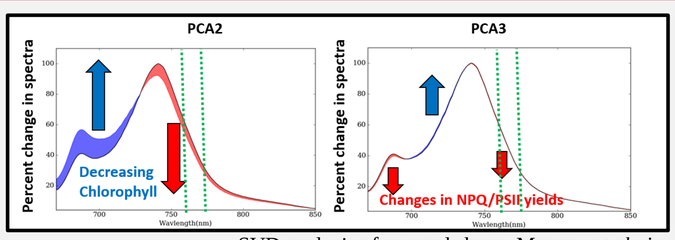

SVD analysis of spectral shape: Magney *et al., in prep.*

Conclusions:

- Changes in the spectral shape of SIF are mostly driven by chlorophyll content, followed by changes in NPQ & PSII yields. See PCA2 and PCA3 from a SVD analysis.

leaf.

Tower approach:

- Build five spectrometers to measure SIF using the Fraunhofer approach
- Currently installed in Costa Rica, Iowa (2), and Colorado.
- Collect species specific and spatially varying information on plant function (SIF, other VIs) every 15 minutes over the course of a season.

Installation: Niwot Ridge, CO

Diurnal data from La Selva, Costa Rica

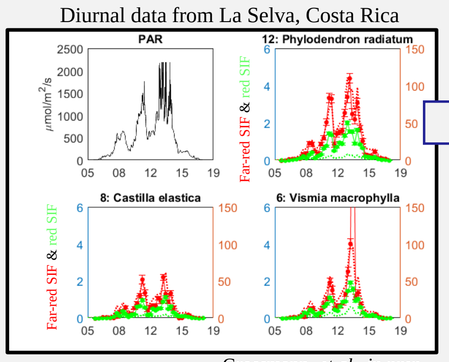

Grossmann, *et al., in prep.*

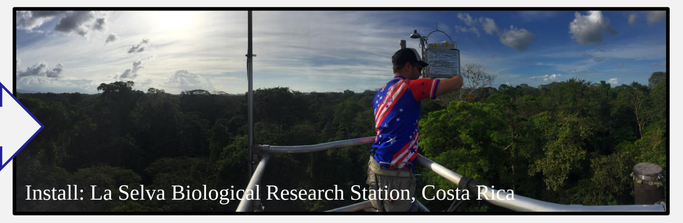

Conclusions:

- Changes in SIF are primarily driven by absorbed photosynthetically active radiation (PAR).
- Currently QA/QC data from the four sites.

tower.

Air approach:

- CFIS was built at JPL and has been flying over a variety of ecosystems since 2015.
- Capture the spatial variability of the SIF signal
- Coincident flights with SMAPVEX campaign and Carnegie Airborne Observatory
- Diurnal flights over flux towers

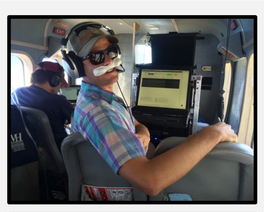

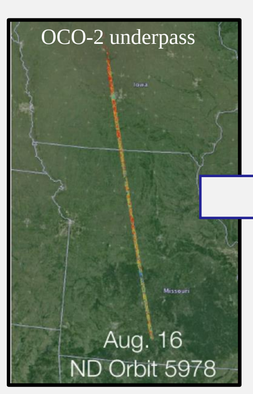

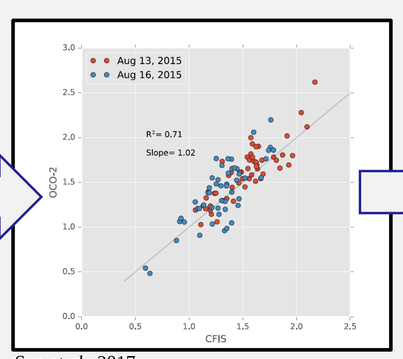

Sun *et al.*, 2017
Frankenberg *et al., in prep.*

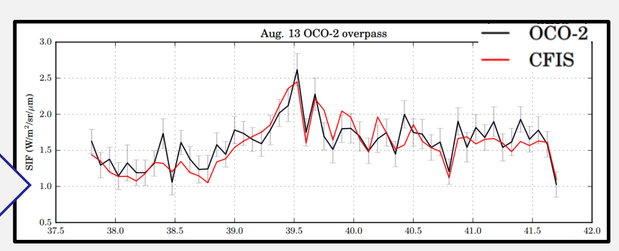

Sun *et al.*, 2017

Conclusions:

- OCO-2 underpass correspond well with CFIS data.
- See poster of P. Koehler for initial retrieval results.

aircraft.

Satellite approach:

- Using information from leaf, tower, and airborne scales to better interpret the spatial, spectral, and temporal variability in the SIF signal.
- Outline of approach is highlighted in Sun et al., 2017.

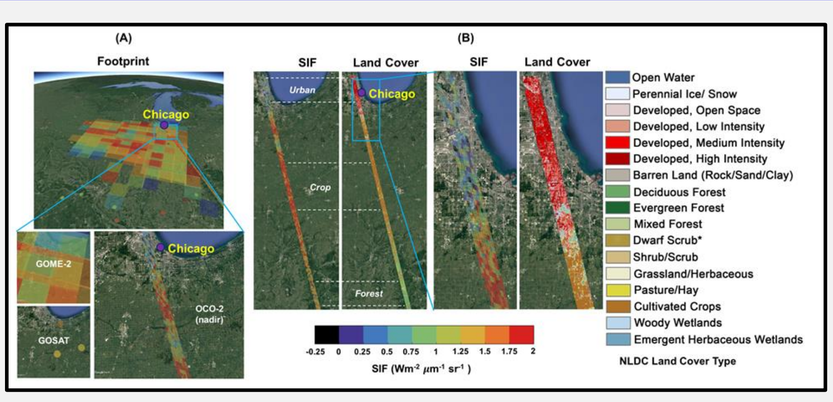

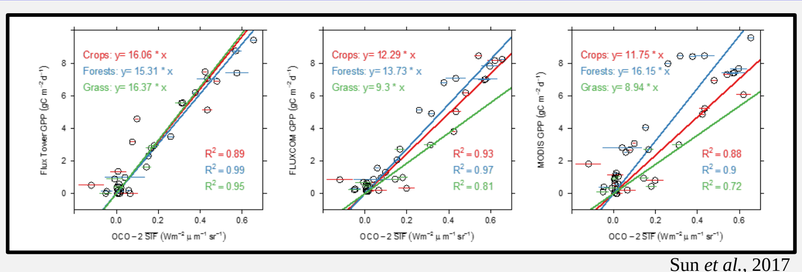

Sun *et al.*, 2017

Conclusions:

- Leaf, tower, and airborne data are enabling improved interpretation of SIF at 757 and 771 nm from OCO-2.

satellite.

National Aeronautics and Space Administration

Jet Propulsion Laboratory
California Institute of Technology
Pasadena, California

Acknowledgements:

This work was supported by a NASA Postdoctoral Program Fellowship awarded to TSM, OCO-2, and the Keck Institute for Space Studies. In addition to the co-authors, thanks goes out to Gretchen North, Nick Parazoo, Thomas Davis, Ulli Siebt, Joe Berry, Albert Porcar-Castell, Darren Drewry, and Ari Kornfield for helpful insights and discussions.

www.nasa.gov

Poster No. EA-10

National Aeronautics and Space Administration

High-resolution mapping of tidal marsh distribution and biomass with L-band radar

Nathan Thomas 334-F
Marc Simard 334-F

1. INTRODUCTION

- Tidal marshes provide important ecosystem services such as carbon storage, coastal protection and biodiversity
- High resolution maps of extent and biomass are required for reporting to UN initiatives (e.g., Intergovernmental Panel on Climate Change (IPCC)) but are largely unavailable
- Anthropogenic pressures such as coastal development are causing the loss of tidal marshes and their associated ecosystem services

2. OBJECTIVE

- Map Louisiana tidal marsh distribution and biomass to satisfy IPCC reporting requirements
  - Derive a high-resolution map of tidal marsh extent
  - Test the capacity for biomass mapping and monitoring with JPL airborne radar

3. MAPPING TIDAL MARSH EXTENT

- Landsat 8 OLI optical satellite imagery
- Scenes acquired August 8th and August 25th 2015 and corrected for temporal/atmospheric effects
- Subset to the parishes of St. Mary's and Terrebonne
- Classified using a Random Forests machine learning algorithm using image segmentation via free and open source software (Fig. 1, Table 1)
- Training provided by in-situ coastal monitoring stations

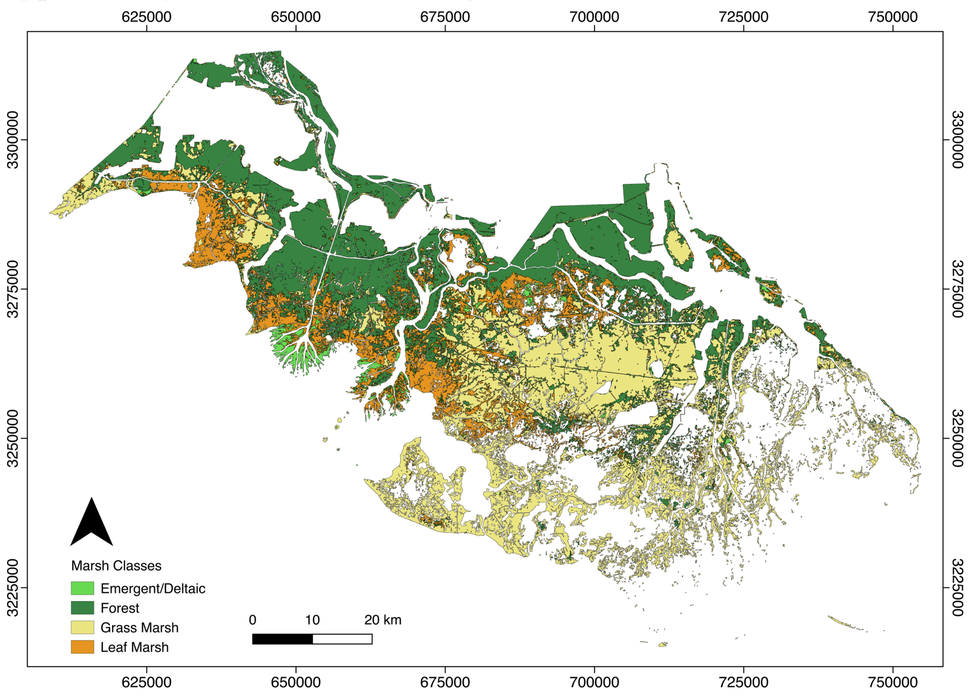

Fig. 1 Landsat 8 classification of Louisiana tidal marsh extent

4. TIDAL MARSH BIOMASS

- NASA JPL Uninhabited Airborne Vehicle Synthetic Aperture Radar (UAVSAR) imagery
- Scenes acquired May 2015 and October 2016
- Radiometric and geometric calibration and merging of adjacent flightlines
- Field data acquired May and September 2015 (low and peak biomass)
- Relationships derived between UAVSAR HV polarized backscatter and field biomass data (Fig. 2)
- May and September field data were combined to derive relationships with each UAVSAR scene
- Backscatter increased with biomass until saturation occurred at high biomass values
- Biomass maps (Fig 3 and Fig 4; Table 1) created by applying derived relationship to UAVSAR HV polarized scenes

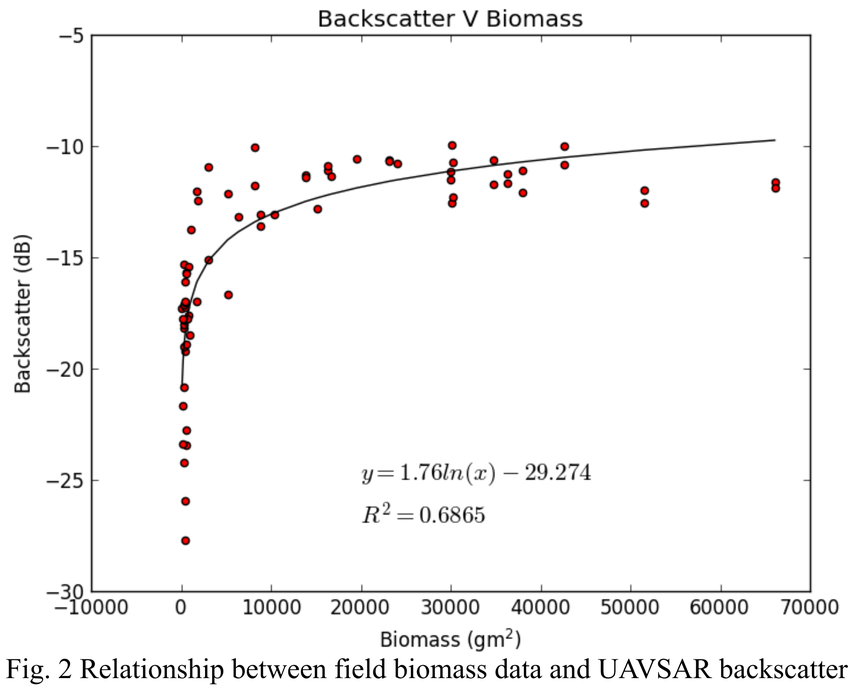

Fig. 2 Relationship between field biomass data and UAVSAR backscatter

5. BIOMASS MAPS

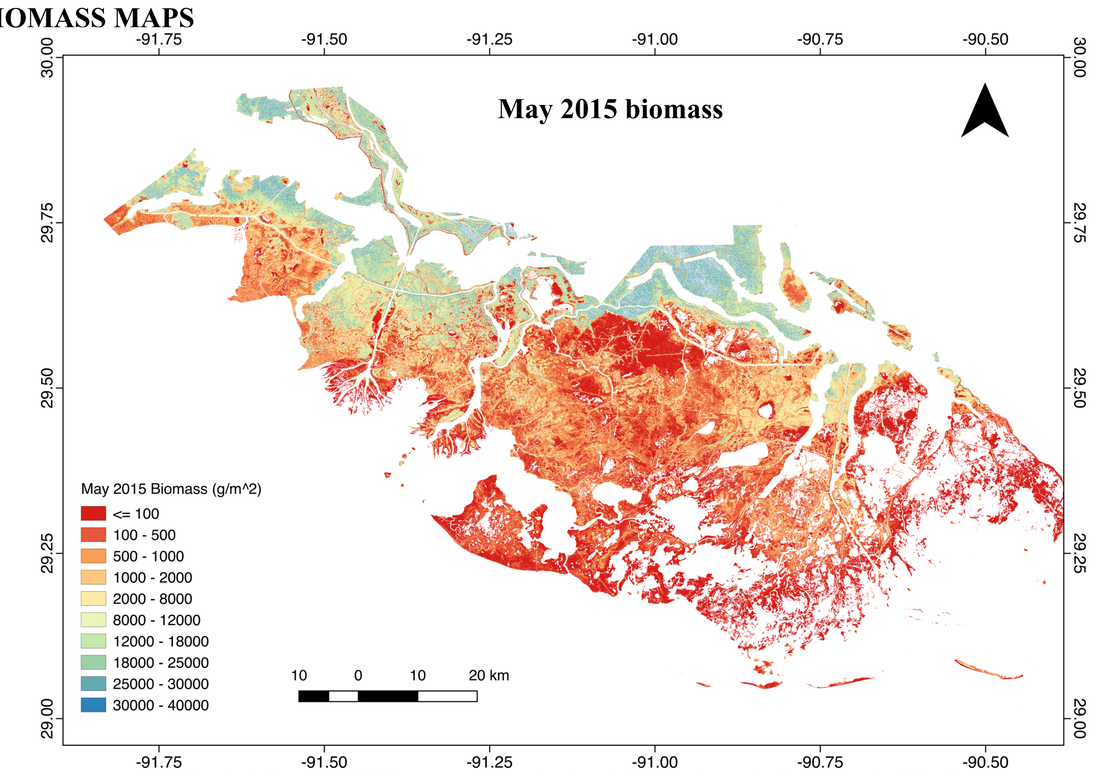

Fig 3. May 2015 biomass map derived from the relationship in Fig 2.

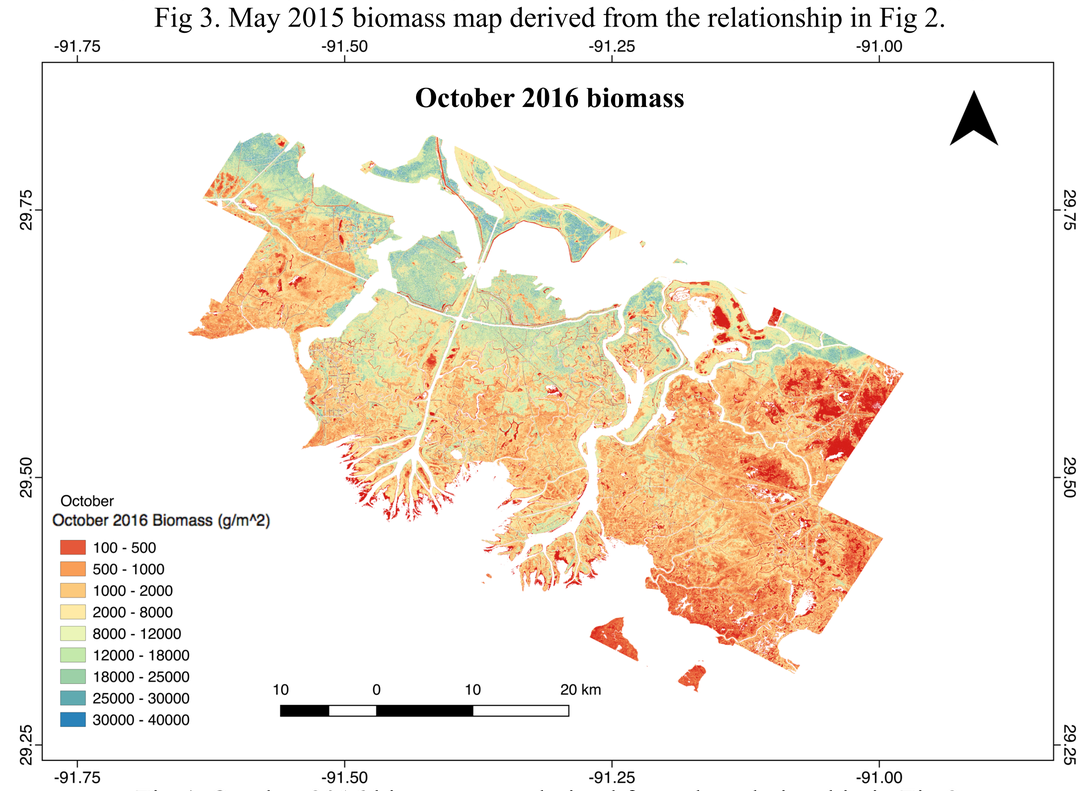

Fig 4. October 2016 biomass map derived from the relationship in Fig 2.

6. SUMMARY OF RESULTS

Table 1. Summary of tidal marsh class are and seasonal biomass values

	Area (km^2)	Oct Biomass (t)	May Biomass (t)	Common Extent Difference (t)
Grass	1,339	608,746	1,700,874	92,431
Leaf	507	890,113	828,760	286,822
Forest	1,288	6,829,973	18,910,317	N/A
Emergent/Delta	76	131,508	85,368	109,972

- Increase in biomass in October, coincident with increased productivity of the marsh vegetation
- Grass marshes are the dominant marsh type
- Seaward increase in the Wax Lake and Achafalaya deltas during peak biomass
- Smallest biomass values amongst the extensive inundated grass marshes

7. DELIVERABLES

- A novel map of Louisiana tidal marsh extent at high resolution, providing a new and up-to-date baseline
- Created previously unavailable very high resolution maps of seasonal biomass which provide greater understanding of the seasonal change in marsh productivity as required for monitoring by the IPCC
- Successfully quantified biomass using JPL UAVSAR, demonstrating the capability for biomass/carbon accounting of coastal marsh ecosystems

8. FURTHER WORK

- Simulations for NASA-ISRO SAR
  - ALOS-2/Landsat
- Carbon estimations and seasonal changes
- Estimations of error propagation

National Aeronautics and Space Administration

Jet Propulsion Laboratory
California Institute of Technology
Pasadena, California

www.nasa.gov

Poster No. EA-11

National Aeronautics and Space Administration

Mapping Forest Height Using PolInSAR and Lidar Fusion

Michael Denbina (334F)
Marc Simard (334F)

1. Introduction

•We used airborne remote sensing data from NASA's Uninhabited Aerial Vehicle Synthetic Aperture Radar (UAVSAR) and Land, Vegetation, & Ice Sensor (LVIS) lidar to map forest canopy height for study areas in the country of Gabon. These data were collected as part of NASA's AfriSAR campaign in 2016.

•We developed a new machine learning-based method to perform data fusion of radar and lidar forest height estimates. The result has the wide coverage area and high spatial resolution of UAVSAR, but with improved accuracy compared to a purely radar-based approach. The forest height maps for the two study areas are shown in Fig. 1.

•Obtaining high resolution maps of forest height is important for understanding the ecosystem carbon budget, and for quantifying the effects of deforestation and forest growth. Forest biomass can be estimated from forest height using allometric equations derived from field measurements.

•Developing methods for fusion of radar and lidar data is vital to make optimum use of data from future spaceborne missions, such as the NASA-ISRO SAR (NISAR) and the Global Ecosystems Dynamics Investigation (GEDI) lidar.

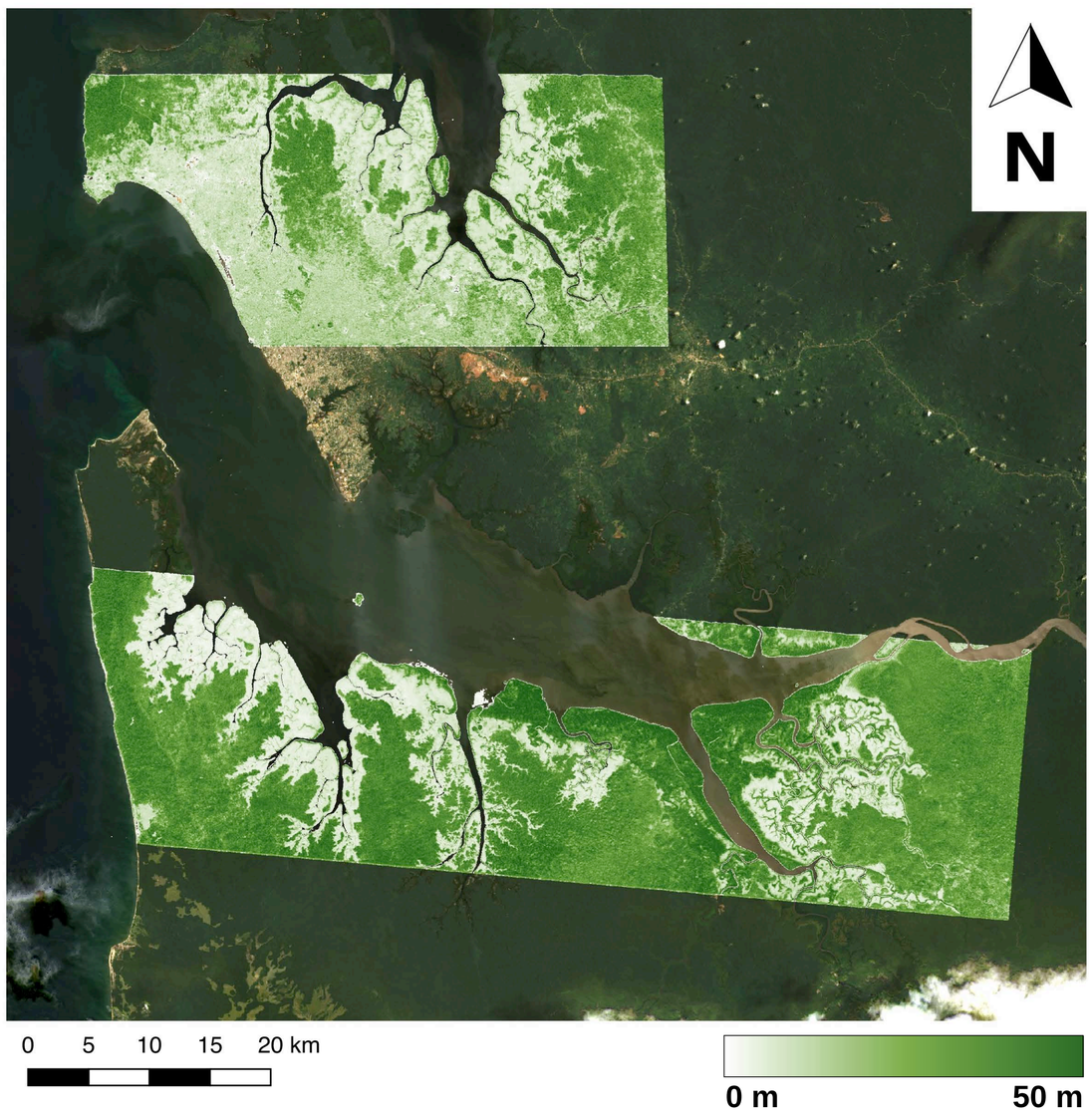

Fig. 1. Forest height maps created using UAVSAR and LVIS machine learning fusion for Akanda National Park (North) and Pongara National Park (South), Gabon. Overlaid on Landsat-8 imagery, available from U.S. Geological Survey.

2. Methods

•We estimate forest height from the UAVSAR data using polarimetric synthetic aperture radar interferometry (PolInSAR) and the random volume over ground (RVoG) forest model, which relates the physical characteristics of the forest to the radar observations.

•For multi-baseline data (i.e., greater than two different flight tracks), we can estimate multiple independent forest height estimates from the various baselines which must then be weighted or selected in order to obtain a single forest height for each radar image pixel. The UAVSAR data contained a large number of repeat passes (5 for Pongara, 9 for Akanda), making baseline selection a vital step in the forest height estimation process.

•We tackled this baseline selection problem using a support vector machine (SVM) classifier with a linear kernel function, using a large feature set which contained a variety of radar-derived metrics based on the PolInSAR coherences and coherence region shape, viewing and terrain geometry, and radar backscatter. A flowchart of the method is shown in Fig. 2.

•The SVM was trained using a sparse subset of the LVIS relative height 100 (RH100) data with 250 m spatial separation between samples. This lidar sampling density is similar to what will be expected from future spaceborne lidar missions, such as GEDI. The remainder of the LVIS data was used for validation (Fig. 3).

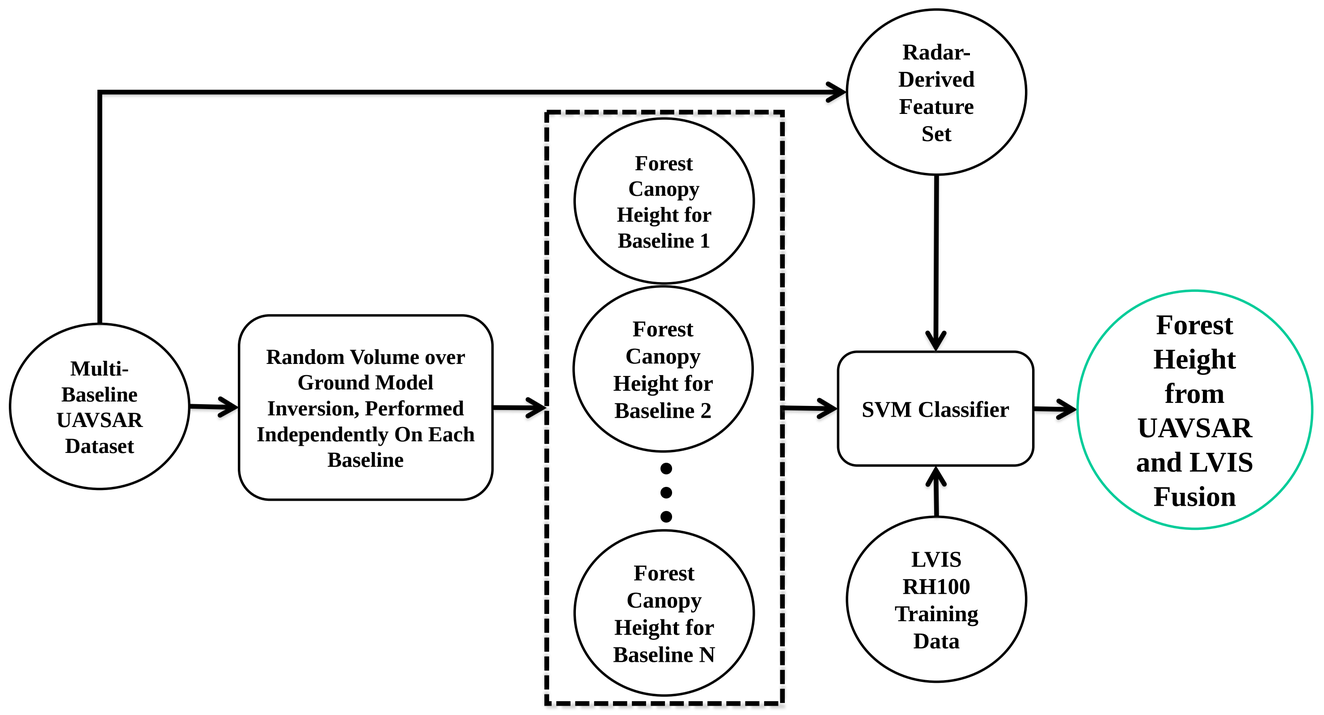

Fig 2. Flowchart of the proposed forest height fusion method.

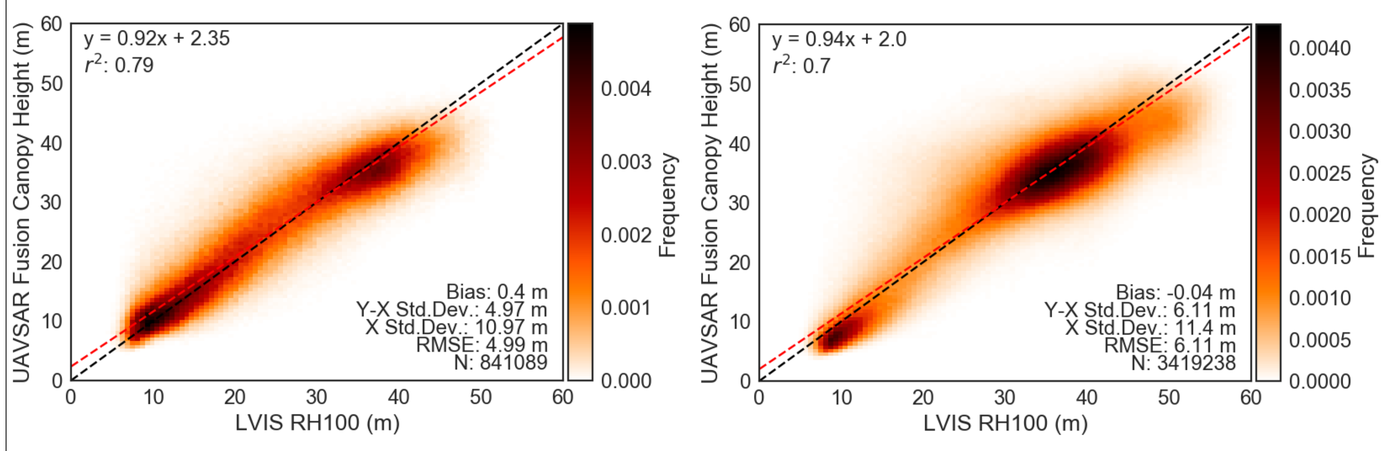

Fig. 3. Density plots of forest height using the proposed fusion method vs. LVIS RH100 forest height. Left: Akanda National Park (Northern area in Fig. 1). Right: Pongara National Park (Southern area in Fig. 1).

3. Conclusions

•Developed a new method for fusion of PolInSAR and lidar data in order to generate more accurate PolInSAR forest height estimates, with a high spatial resolution (30 m) and a wide coverage area (22 km swath). The method considers the PolInSAR baseline selection process as a supervised classification problem, which we perform using a support vector machine classifier trained with sparsely distributed lidar-derived forest heights.

•Produced forest height maps for two national parks in the country of Gabon. Results validated using LVIS samples excluded from the data fusion procedure, with RMSE of 4.99 m in the Akanda National Park study area, and 6.11 m in the Pongara National Park study area. For comparison, we also performed baseline selection using standard radar-derived data quality metrics (coherence region eccentricity, and expected phase center height variance), but these methods resulted in less accurate forest height estimates (RMSE values of 8.47 m for Akanda and 7.69 m for Pongara).

•Results demonstrate the potential for fusion of PolInSAR and spaceborne lidar data. Lidar sample spacing of 250 to 500 m is sufficient for training the SVM classifier. Data from the Global Ecosystem Dynamics Investigation (GEDI) lidar will satisfy this requirement, though the data is expected to be noisier than the LVIS airborne lidar data used in this study.

•Next Steps: Continue to refine methodology, and apply the method to other datasets and study areas. Validate using field data in Pongara National Park. Estimate biomass from forest height maps using allometric equations.

National Aeronautics and Space Administration

Jet Propulsion Laboratory
California Institute of Technology
Pasadena, California

www.nasa.gov

Poster No. EA-12

National Aeronautics and Space Administration

Modelling Surface Water Flow on Coastal Wetlands

Ke Liu (334F)
Marc Simard (334F)

1. INTRODUCTION

Coastal wetlands are valuable natural resources with multiple ecological and economic functions. They provide an effective storage of carbon, a natural habitat for many endangered species and a defense line against storm surges and waves.

Louisiana has the largest area of coastal wetlands in the contiguous United States. While most of the Louisiana coastline is struggling with marsh erosion and land loss, two river deltas, the Wax Lake Delta and the Atchafalaya Delta, are emerging in the Atchafalaya Bay and provide a unique setting to study the interaction of river and coastal hydrodynamics.

JPL researchers conducted field campaign over the Atchafalaya Basin in 2016 and collected data to show the water flow on the wetlands was dynamically changing with tides and river flow, but the temporal resolution of the measurement data was limited during the survey period of time.

In this project, we develop numerical models to bridge the gaps between discrete measurements and utilize the models and the measurement data to better understand the surface water flow on the coastal wetlands.

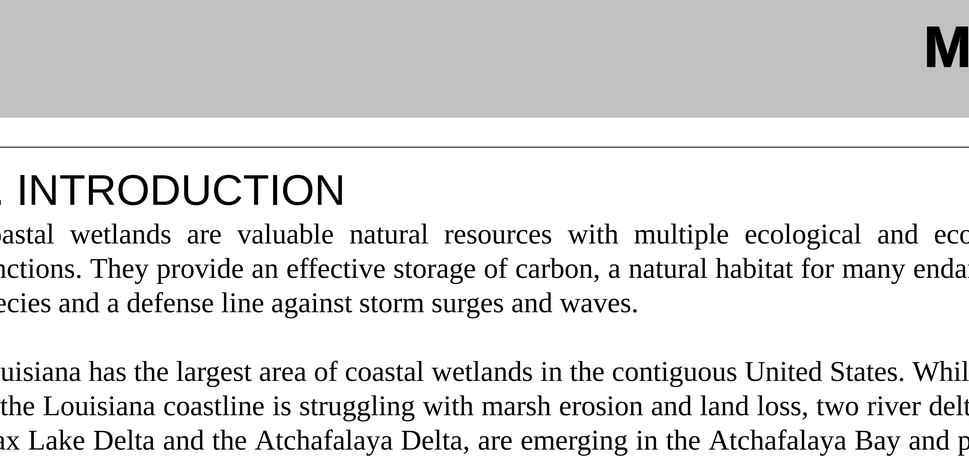

Figures 1. The study area on the Louisiana coast.

2. METHODS

The water depth measured by SONAR is interpolated to reconstruct the river bathymetry in the Wax Lake Outlet.

A 1D model is developed for the Wax Lake Outlet to study the interaction of tides and river flow using HEC-RAS, and a depth-averaged model is developed using Delft3D for the whole Atchafalaya Basin to simulate the water level change on the wetlands and the water exchange between the wetland and the river channel.

The model results are compared with the water level and the water surface profiles measured during the field campaign. The difference between the model results and the observations is used to infer the probability distributions of model parameters and identify key physical processes which has a significant impact on the modelled results.

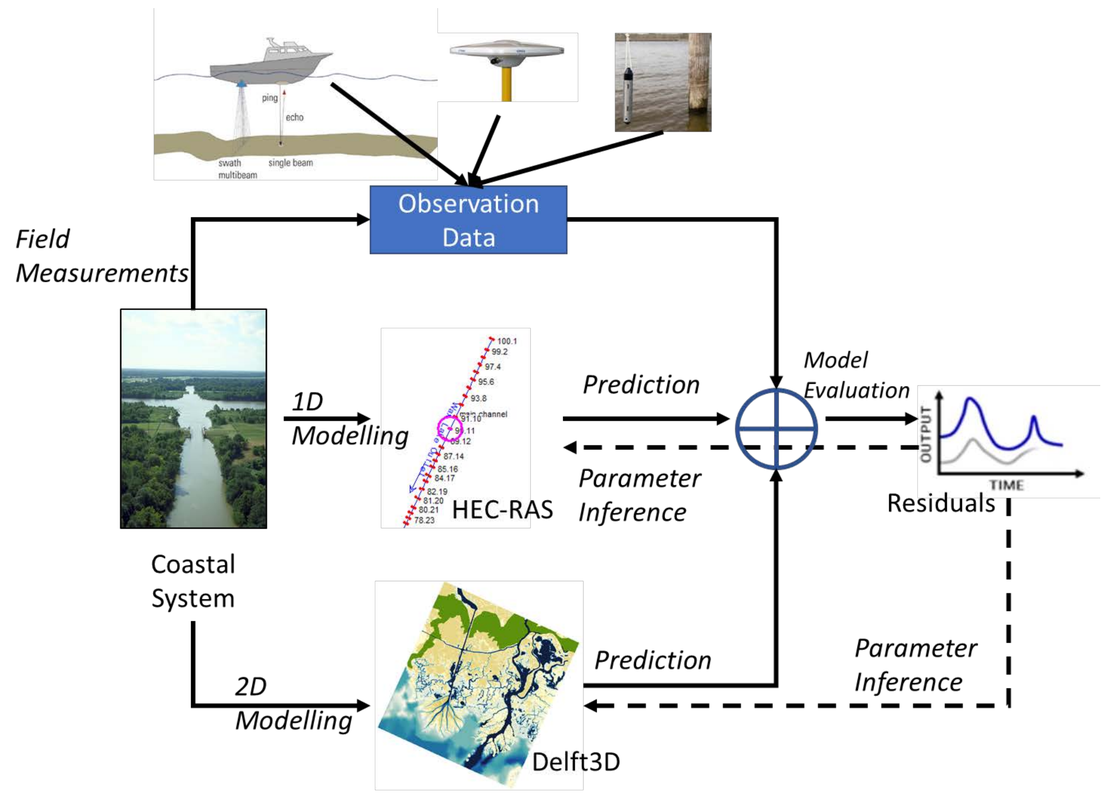

Figure 2. The flow chart of our methods to merge the models and the observation data.

3. RESULTS

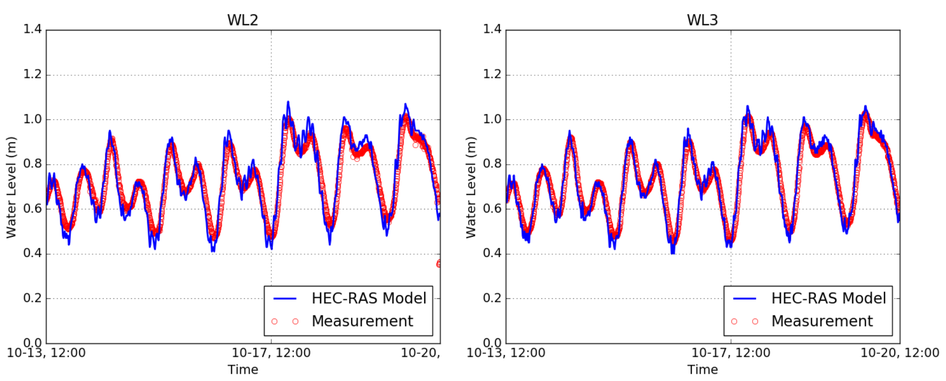

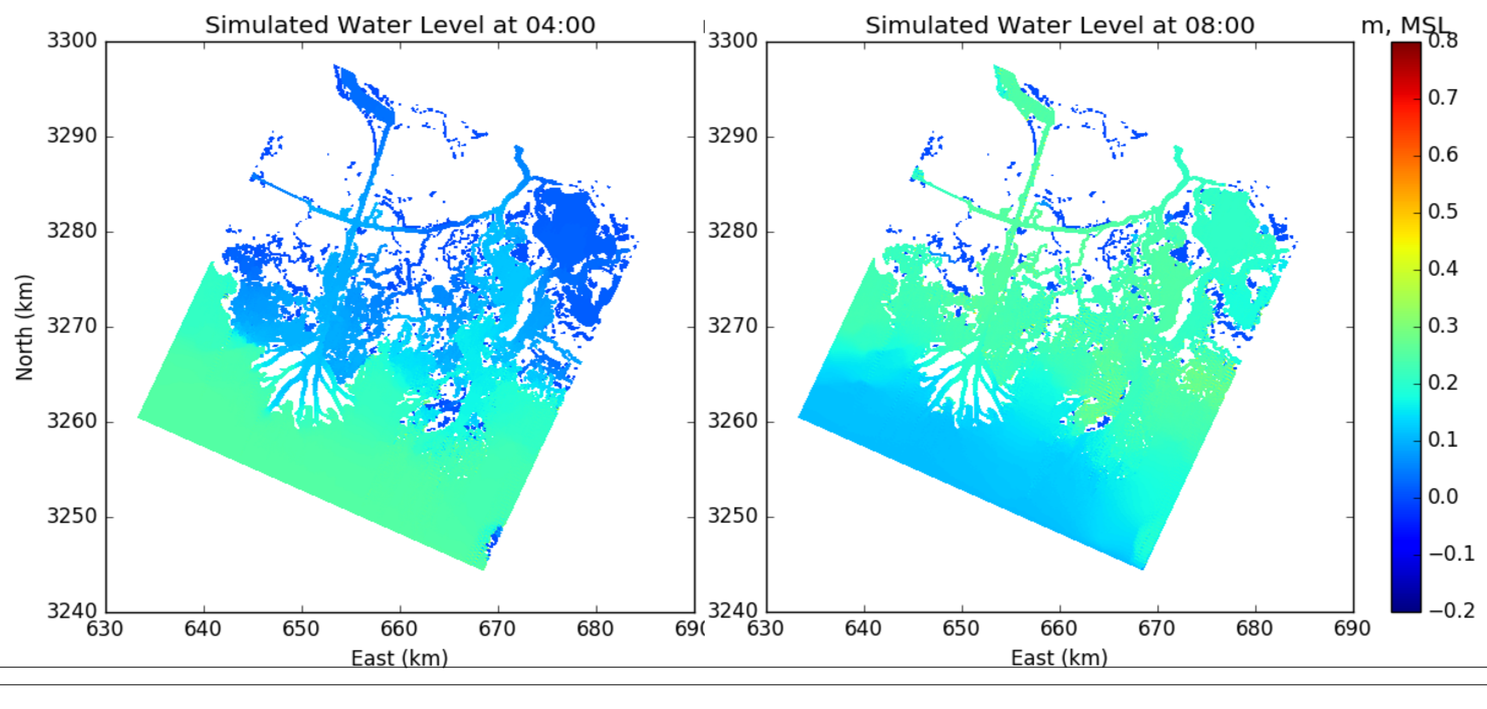

Figure 3. Left: A comparison of modelled tidal variation from HEC-RAS and the observation data at water gauges.
Right: The modelled water level in the Atchafalaya Basin from Delft3D.

4. CONCLUSIONS

- We measured river bathymetry, water level changes and water surface profiles in the Atchafalaya Basin.
- We integrated the measurements from different instruments and developed numerical models (1D and 2D) to simulate the hydrodynamic processes in the Wax Lake Outlet and the adjacent wetlands.
- The difference between model results and the observations was utilized to infer the optimum model setting using Bayesian methods.
- The optimized 1D model not only successfully reproduced the measured water level in the Wax Lake Outlet and the water surface profiles along the channel, but also helped identify the key parameters and processes which play significant roles in the 2D hydrodynamics.
- The 2D model predicted the water level variation in the Atchafalaya Basin under different riverine and marine forcing and served as a useful tool to better understand surface water flow on coastal wetlands in a complicated geophysical setting.

National Aeronautics and Space Administration

Jet Propulsion Laboratory
California Institute of Technology
Pasadena, California

www.nasa.gov

Poster No.: EA-13

National Aeronautics and Space Administration

SAR Interferometry for Surface-Water Level Change in Mississippi Wetlands

Tien-Hao Liao (334F)
Marc Simard(334F)

Background

Wetlands connect land and water with productive ecosystems. It plays like buffer by collecting water and releasing it slowly to reduce flooding. For areas with continual inundation, surface-water level change is an index to monitor the overall water throughput of the wetlands. Here we study surface-water change over grassy wetlands such as marsh. L-band (wavelength~24cm) radar interferometry is capable to capture its typical variation, few to tens centimeters. This study includes forward modelling, radar imaging processing, and in-situ validation.

Method

For cylinders over flat water surface at L-band, strong double-bounce scattering is dominant.

- Through HH polarization monte-carlo simulation is applied to derive the relation between interferometric phase change and surface water level change, vertical displacement.
- ISCE(InSAR Scientific Computing Environment) software is used to process interferogram with speckle noise reduction.
- Retrieve water level change through adjacent pairs of interferogram in time-series.

$$\Delta WL = \Delta\phi/(2k\cos\theta)$$

- For larger time period, accumulate the retrieved water level change.

$$\Delta WL_{1,3} = \Delta WL_{1,2} + \Delta WL_{2,3}$$

Processing Flow Diagram

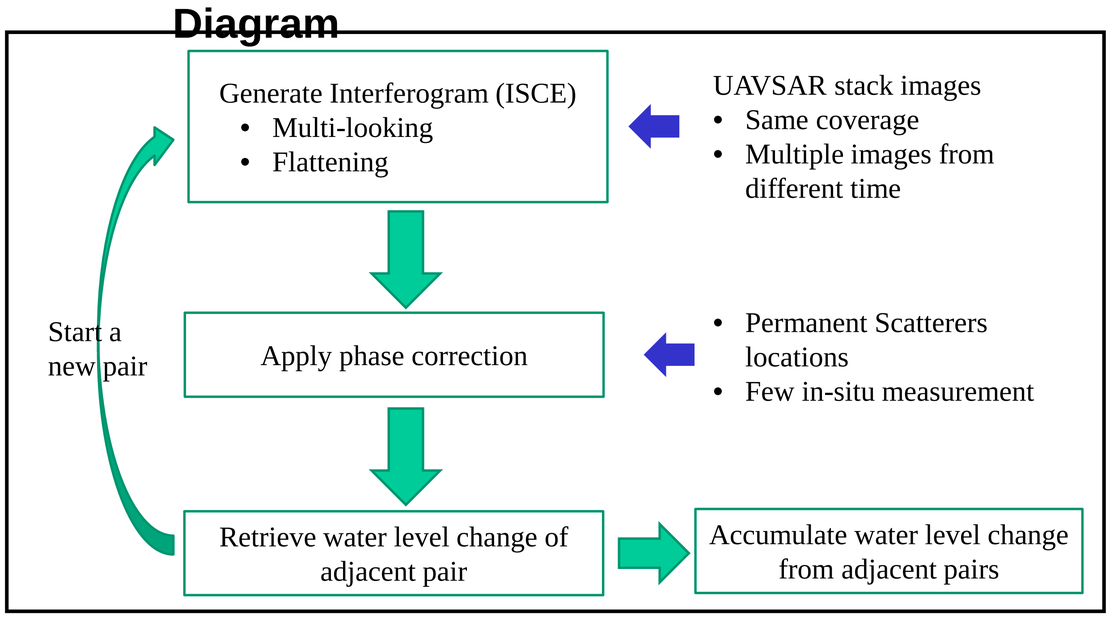

UAVSAR gulfco 12011 Acquisition, Oct.17,2016 (~4min/track)

Stack-track	Track 7	Track 8	Track 9	Track 10	Track 11	Track 12
Starting Time	14:27	14:56	15:25	15:54	16:22	16:51

UAVSAR gulfco 12011 coverage(S-E bound)

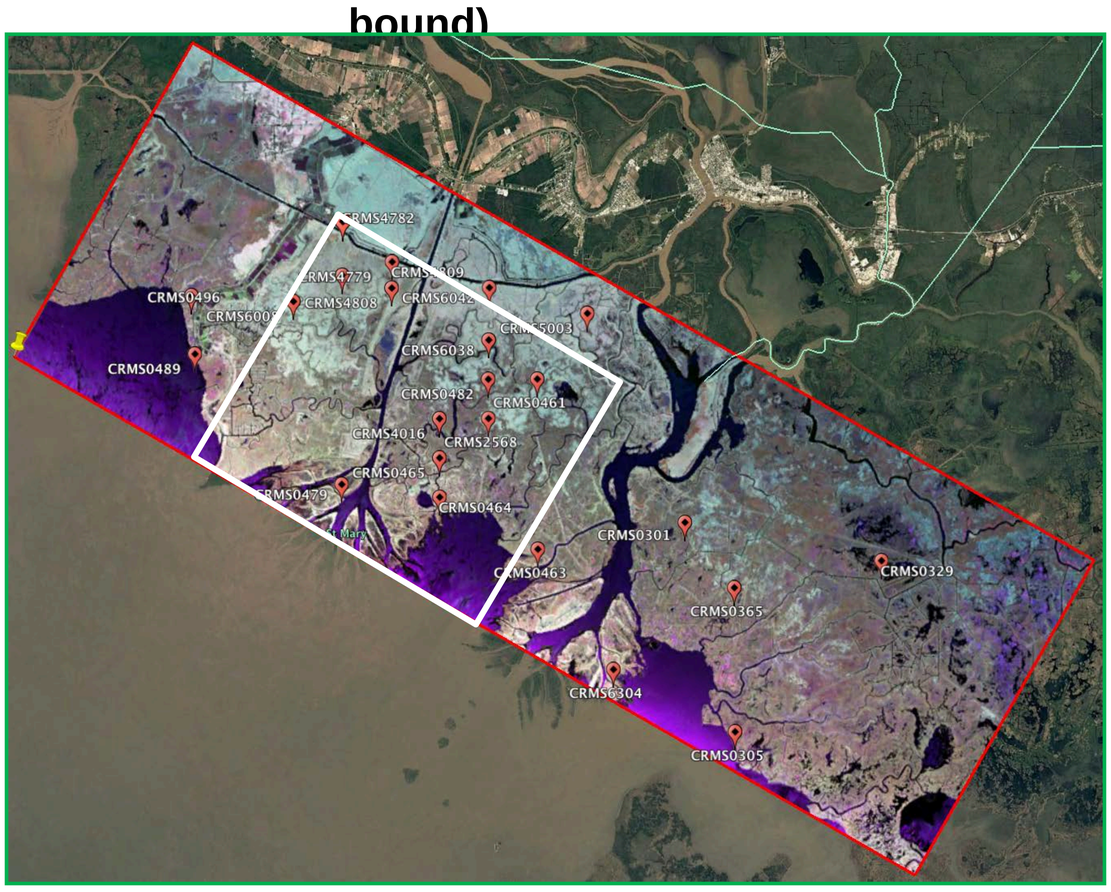

Radar data dependency

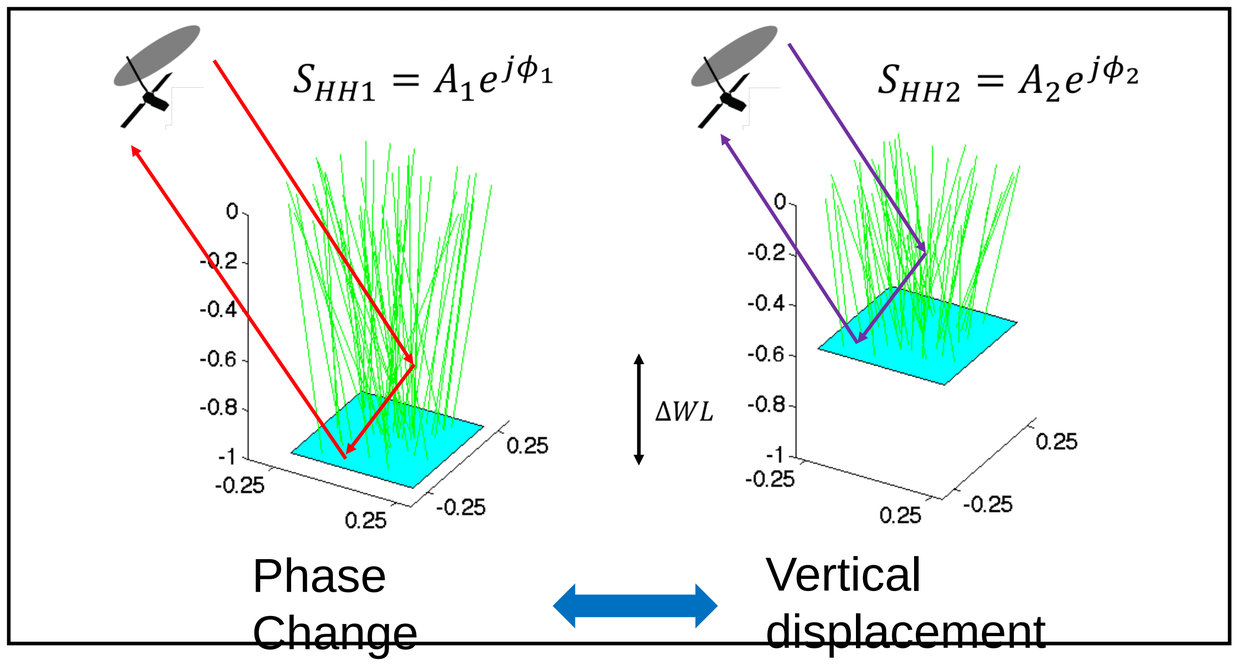

Results

Apply the model to wetlands around Atchafalaya Basin in Louisiana. For radar imaging, L-band single look complex stacks(SLC stacks) from NASA/JPL UAVSAR (Uninhabited Aerial Vehicle Synthetic Aperture Radar) is applied. The acquisition period applied here is Oct.17, 2016. Hourly in-situ water level data from CRMS (Coastwide Reference Monitoring System) stations are applied.

Time-series phase change

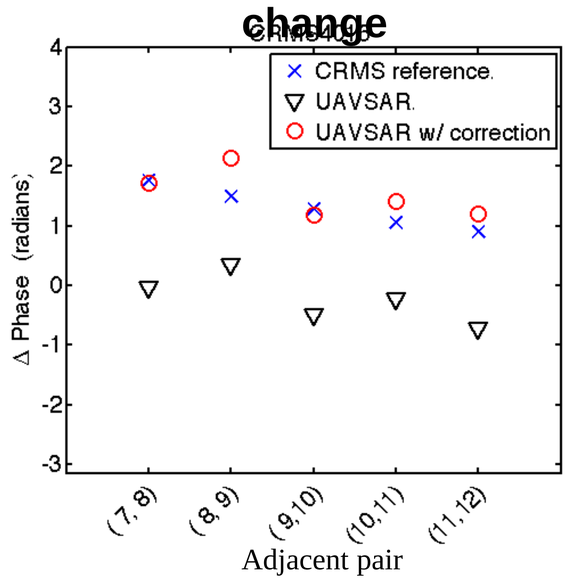

Time-series Water Level Retrieval

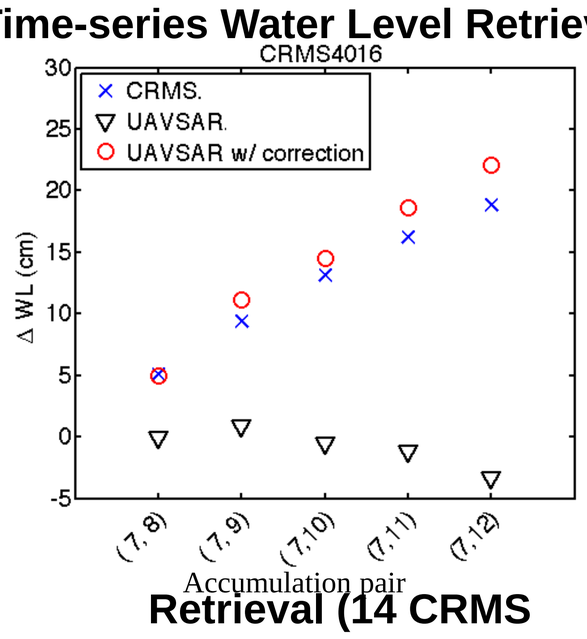

In-situ measurement

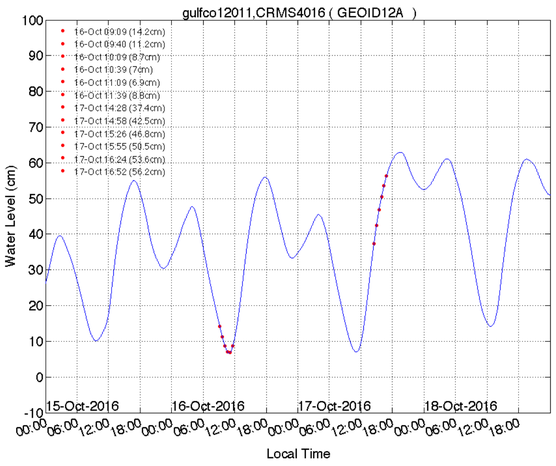

Retrieval (14 CRMS sites)

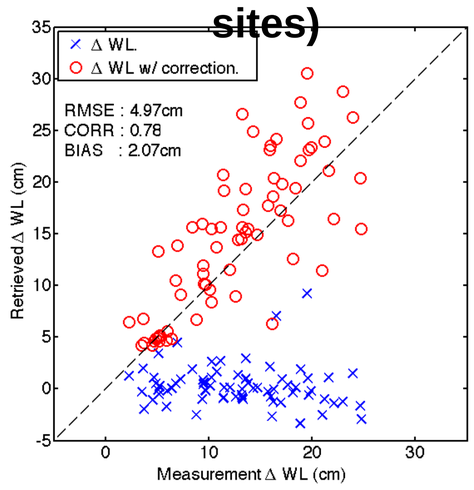

Map pair(Track7,Track12), ~2hr 30min duration, rising tide

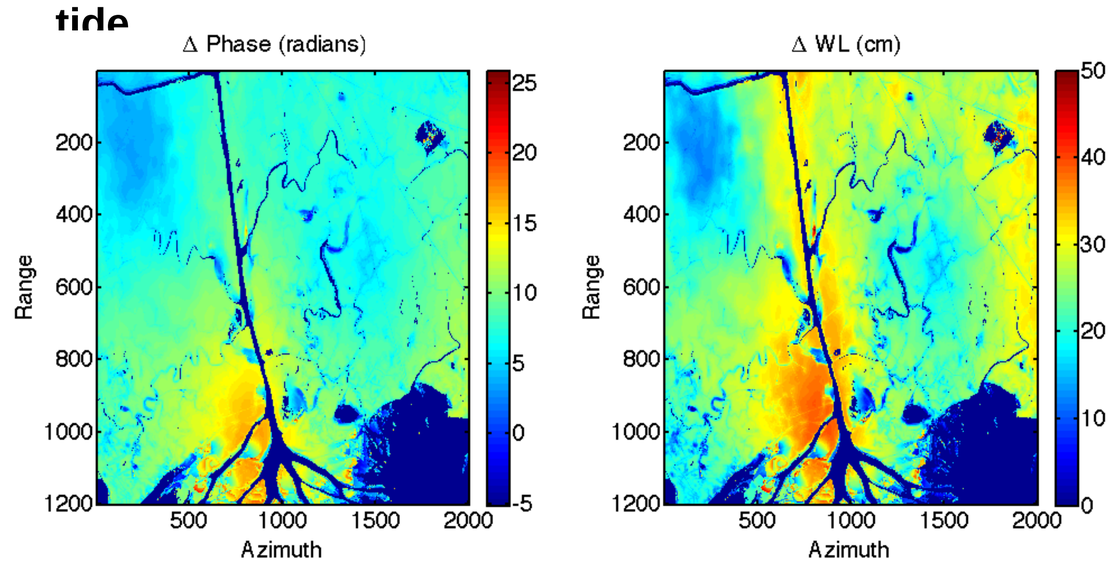

National Aeronautics and Space Administration

Jet Propulsion Laboratory
California Institute of Technology
Pasadena, California

www.nasa.gov

Poster No.EA-14

Efficient Modeling of Electromagnetic Scattering by Large and Complex-Geometry Snow Particles

Ines Fenni*, Ziad S. Haddad*, Hélène Roussel, Raj Mittra#**

*** Radar Science (334H), Jet Propulsion Laboratory, USA ** UPMC Univ Paris 06, UR2, L2E, F-75005, France, # EMC Lab , University of Central Florida, USA and King Abdul Aziz University, Saudi Arabia**

National Aeronautics and Space Administration

I – Introduction :

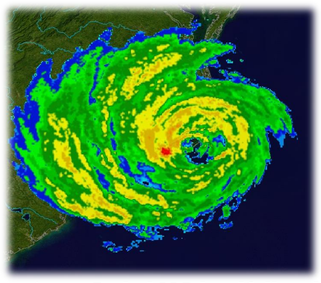

Hurricane Isabel NC landfall radar

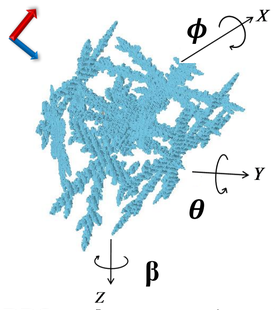

With DDScat the target orientation (to) is defined using the Euler angles.

Scattering by large and complex-shaped ice particles

NEED — Calculate the scattering properties of **snowflakes of various sizes and shapes**.

AVAILABLE NOW — **Discrete Dipole approximation** (**DDA**) : DDScat, ADDA, …

WHY NOT — Characteristic Basis Function Method (Direct Solver-based method)

DDScat

$$\langle Q \rangle = \frac{1}{8\pi^2}\int_0^{2\pi} d\beta \int_{-1}^{1} d\cos\theta \int_0^{2\pi} d\phi \; Q(\beta,\theta,\phi)$$

CBFM-based code

$$\langle Q \rangle = \frac{1}{4\pi}\int_0^{2\pi} d\phi_i \int_0^{\pi} \sin\theta_i \; d\theta_i \; Q(\phi_i,\theta_i)$$

Direct solver $\quad \boldsymbol{Z E = E^{inc}}$

II – Application of the CBFM to the problem of scattering by complex particles :

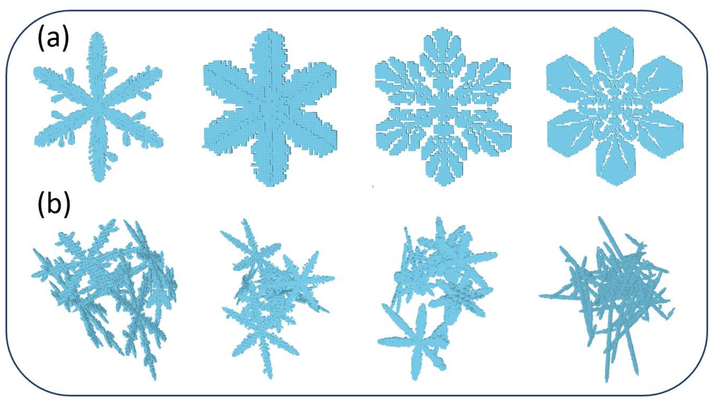

Pristine crystals **(a)** simulated using the snowflake algorithm [1] and aggregate snow particles **(b)**

Frequencies of interest : 15 - 200 GHz

OpenSSP database [1] :

- **6646 particles : pristine crystals and aggregate snow particles**
- **50 µm resolution**
- **Available input shape files for DDScat**

1) Integral representation of the total electric field (EFIE) [2] :

VIEM : $\bar{E}(\bar{r}) = \bar{E}^{inc}(\bar{r}) + \left(k_0^2 + \nabla\nabla.\right)\int_\Omega \chi(\bar{r}')\,\bar{\bar{G}}(\bar{r},\bar{r}')\,\bar{E}(\bar{r}')\,d\bar{r}'$

$\Rightarrow \boxed{\bar{\bar{\Gamma}}\bar{E}(\bar{r}) = \bar{E}^{inc}(\bar{r})}$ where $\bar{\bar{\Gamma}} = \bar{\bar{I}} - \left(k_0^2 + \nabla\nabla.\right)\int_\Omega \chi(\bar{r}')\,\bar{\bar{G}}(\bar{r},\bar{r}')\,d\bar{r}'$

Method of Moments

The particle is discretized into $\mathbf{Nb_c}$ cubic cells Ω_n ,of side $c_n \leq \frac{\lambda_s}{10}$; $\lambda_s = \frac{\lambda_0}{\sqrt{Re(\varepsilon_r)}}$

$\Rightarrow \boldsymbol{Z\,E = E^{inc}}$ where **Z** is the **$3Nb_c$ x $3Nb_c$ full matrix** representing the EM interactions inside the particle.

2) Application of the Characteristic Basis Function Method (CBFM) [3] :

Generation of the CBFs

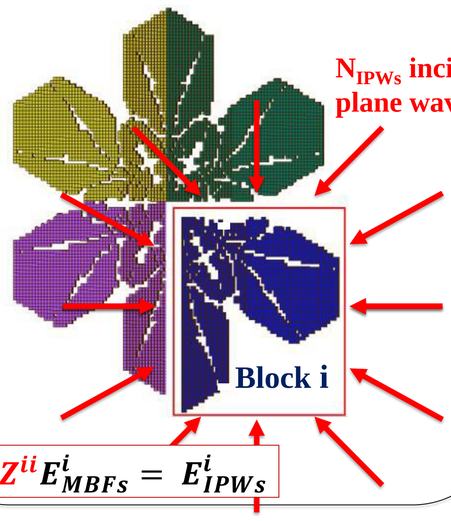

Computation of Z^c

Example : M = 4 blocks

$$Z^c = \begin{pmatrix} C^{(1)t} Z_{11} C^{(1)} & \cdots & C^{(1)t} Z_{14} C^{(4)} \\ C^{(2)t} Z_{21} C^{(1)} & \cdots & C^{(2)t} Z_{24} C^{(4)} \\ \vdots & \ddots & \vdots \\ C^{(4)t} Z_{41} C^{(1)} & \cdots & C^{(4)t} Z_{44} C^{(4)} \end{pmatrix}$$

$K = S_1 + S_2 + S_3 + S_4 \ll 3*N$

$\Rightarrow \boxed{Z^c\,\alpha = E^{c,inc}}$

Compression rate $CR = \dfrac{size\ of\ Z^{MoM}}{size\ of\ Z^c}$

3) Computationally efficient calculation of the CBFs :

1. Sparse representation (SR) of the Macro-Basis Functions

$$\tilde{Z}^{ii}E^i_{MBFs} = E^i_{IPWs}$$

where $\tilde{Z}^{ii}_{l,c} = 0$ if $|Z^{ii}_{l,c}| \leq |Z^{ii}_{1,1}|/f_{SR} \quad l,c \leq 3Nb_c$

f_{SR} is a threshold factor used to down-select the elements of $\mathbf{Z^{ii}}$ whose magnitudes are significant compared to $|\mathbf{Z^{ii}}_{1,1}|$.

\+ **Sparse Direct Solver**

⇒ Makes possible the use of **larger blocks** so a **higher CR**

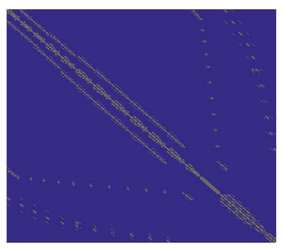

(c) $|\tilde{Z}^{ii}|$ with $f_{SR} = 20$

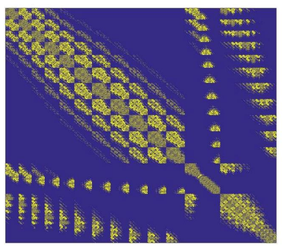

(d) $|\tilde{Z}^{ii}|$ with $f_{SR} = 4x10^2$

2. The Sherman-Morisson-Woodburry Formula-based algorithm

$$Z^{ii}E^i_{MBFs} = E^i_{IPWs}$$

- To solve the local EM problem, we apply a **multi-level Sherman-Morisson-Woodburry Formula-based algorithm** (SMWA) **[4].**
- The Sherman-Morrison Formula provides an explicit formula of the inverse of $\boldsymbol{A = B - uv^t}$

$Z =$

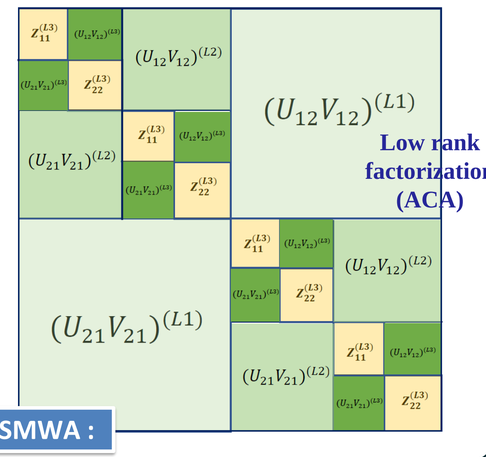

Low rank factorization (ACA)

3-Levels SMWA :

III – Numerical analysis :

We calculate orientation averaged **extinction, scattering and backscattering efficiencies** with the DDA-based code **DDScat** and our full wave CBFM-based model **NESCoP** (Numerically Efficient Scattering by Complex Particles)

Shared Memory worstation

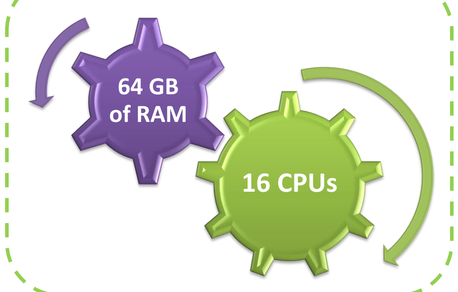

Relative 'difference' (per frequency)

$$E_{r,t}(\%) = 100 \times \frac{|Q_{t,NESCoP} - Q_{t,DDScat}|}{|Q_{t,DDScat}|}$$

Impact of the SMWF-based algorithm on the computational cost and accuracy of NESCoP

a_p = 0.89 mm; d_m=6 mm;
15 ≤f ≤ 150 GHz
0.27 ≤ x_p ≤ 2.79 |m|kd ≤ 0.37
Nb_c =24385 cells

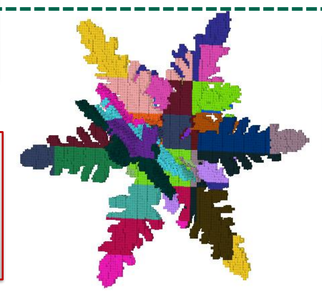

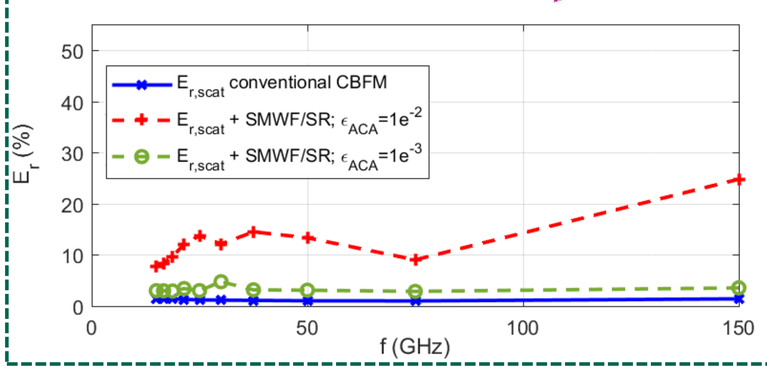

h_B ⇢ Nb_i	0.8 mm ⇢ 1175	3 mm ⇢ 6788		
ε_{ACA}	--	--	1e^{-2}	1e^{-3}
CR	39	166	164	164
Size of Z^c	1866	440	446	445
CBF (min)	8	136	5	18
$(Z^c)^{-1}$ (min)	21	0.4	1	0.5

The scattering efficiencies of the snow aggregate a0013 are averaged over **2700 incident directions (id) @ f = 150 GHz** when the aggregate is divided into **27 and 4 blocks.**

a0000
a_p = 1.61 mm;
d_m=11.45 mm;
16 ≤f ≤ 200 GHz
0.56 ≤ x_p ≤ 6.74
|m|kd ≤ 0.37
Nb_c =140896 cells

165

faster than DDScat

In addition to its higher numerical efficiency, NESCoP converges faster (in terms of to/id) than DDScat.

TABLE : CPU time (min) needed by NESCoP, with 1L and 2L CBFM-E, and DDScat to calculate averaged scattering by a0006 with 703 and 2701 **id** and 900 and 1800 **to** for 16.67 GHz ⩽ f ⩽ 200 GHz.

	1 id/to	703 id	900 to	1800 to	2701 id
1L CBFM-E	126.72	527.67	–	–	1706
2L CBFM-E	329.47	532.15	–	–	1034.87
DDScat	266	–	39207	⩾ 85860	–

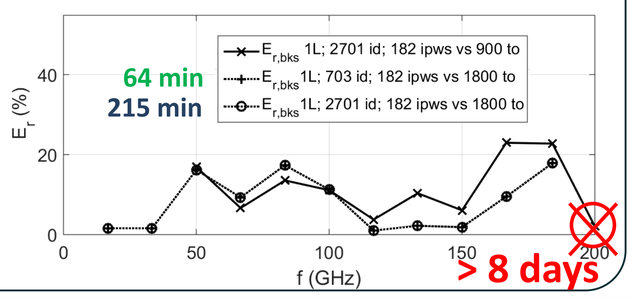

> 8 days

National Aeronautics and Space Administration

Jet Propulsion Laboratory
California Institute of Technology
Pasadena, California
www.nasa.gov

References : [1] Kuo & al. (2016). The Microwave Radiative Properties of Falling Snow Derived from Nonspherical Ice Particle Models. Part I: An Extensive Database of Simulated Pristine Crystals and Aggregate Particles, and Their Scattering Properties. Journal of Applied Meteorology and Climatology, 55(3), 691-708. [2] Fenni & al. "Fast analysis of large 3-D dielectric scattering problems arising in remote sensing of forest areas using the CBFM." IEEE Transactions on Antennas and Propagation 62.8 (2014): 4282-4291 . [3] Lucente & al. "An iteration-free MoM Approach Based on Excitation Independent Characteristic Basis Functions for Solving Large Multiscale Electromagnetic Scattering Problems", IEEE Trans. Antennas Propag., Vol. 56, no. 4, pp.999-1007, Apr. 2008. [4] Chen, & al, "Accelerated Direct Solution of EM Scattering via CBFM With Sherman-Morrison-Woodbury Formula-Based Algorithm," IEEE Transactions on Antennas and Propagation, Oct. 2016.

EA-15

National Aeronautics and Space Administration

Automated generation of large-scale moderate-resolution forest height and disturbance maps for NISAR-like missions

Author: Yang Lei (335F)
Advisor: Robert Treuhaft (335F)

Introduction

- Large-scale moderate-resolution (few- to sub-ha) products of forest height and disturbance are essential for understanding the global carbon distribution as well as its changes in response to natural events and human activities.
- Regarding this scientific need, the NASA-ISRO's NISAR mission is going to be launched in 2021. New methods using dual-pol (HH and HV) small-baseline InSAR observations have been developed for spaceborne repeat-pass InSAR missions like NISAR and also automated by designing a Python software (*https://github.com/leiyangleon/FSH/*) that seamlessly works with JPL's InSAR processing software (ROI_PAC and ISCE).
- For the first time, a mosaic of forest height was generated for Maine and New Hampshire using JAXA's ALOS-1/-2 HV-pol InSAR data and compared with airborne lidar and field inventory data over both flat and mountainous areas. With the HH-pol InSAR data, forest disturbance such as selective logging is not only detected but also quantified in subtropical forests of Australia (compared against NASA's Landsat).

Methodology

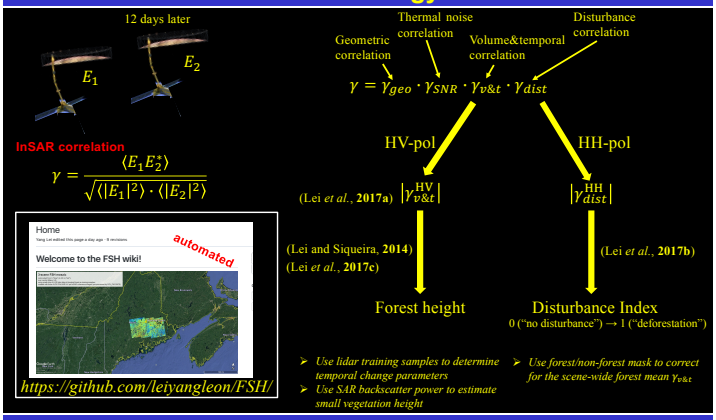

Forest height results

Two-state Forest Height Mosaic

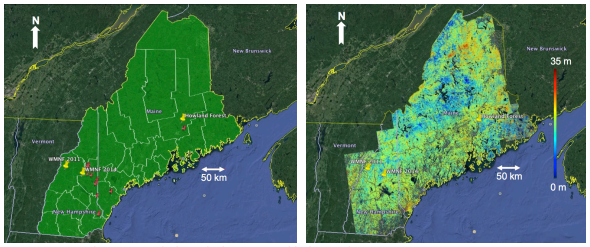

Comparison with airborne lidar data

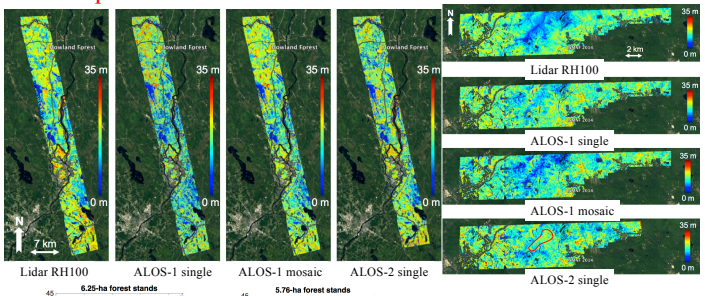

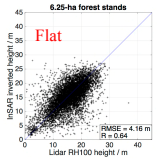

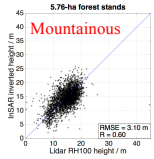

To improve resolution/accuracy
- Multiple-scene mosaicking
- Shorter temporal baseline

Comparison with field measurement

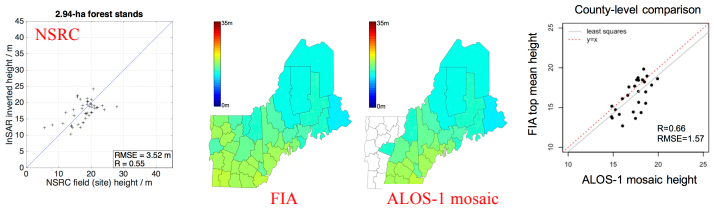

Forest disturbance results

Forest height map (HV-pol data)

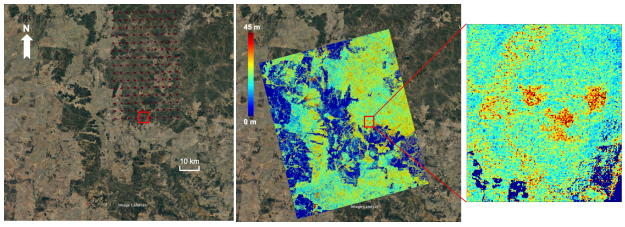

Forest disturbance map (HH-pol data)

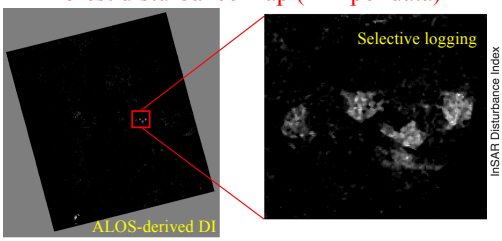

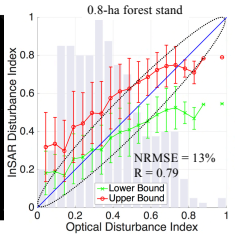

Comparison with Landsat-derived DI data

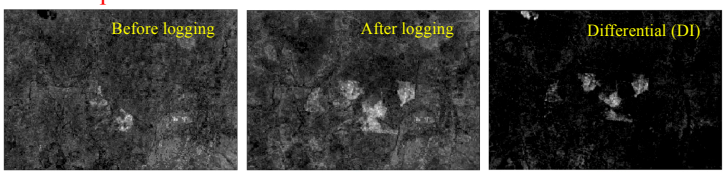

Conclusions

- These new methods enable the automatic retrieval of forest height and disturbance from NISAR-like spaceborne repeat-pass missions for the very first time, which partially relieves the burden of launching the twin satellite (~$500M) to form a tandem mission (state of the art) for this type of study.
- Although easily affected by precipitation, the operational simplicity and efficiency make these methods a potential observing prototype for NISAR-like missions as they are particularly designed for data with single and small spatial baseline, dual polarization, moderate/large temporal baseline, complicated underlying topography.

References

Lei, Y. and Siqueira, P., **2014**. Estimation of forest height using spaceborne repeat-pass L-Band InSAR correlation magnitude over the US State of Maine. *Remote Sensing*, *6*(11), pp.10252-10285.

Lei, Y., Siqueira, P. and Treuhaft, R., **2017a**. A physical scattering model of repeat-pass InSAR correlation for vegetation. *Waves in Random and Complex Media*, *27*(1), pp.129-152.

Lei, Y., Lucas, R., Siqueira, P., Schmidt, M. and Treuhaft, R., **2017b**. Detection of forest disturbance with spaceborne repeat-pass SAR interferometry. (*to be submitted*)

Lei, Y., Siqueira, P., Torbick, N., Ducey, M., Chowdhury, D., Salas, W., **2017c**. Generation of large-scale moderate-resolution forest height mosaic with spaceborne repeat-pass SAR interferometry and lidar. (*to be submitted*)

National Aeronautics and Space Administration
Jet Propulsion Laboratory
California Institute of Technology
Pasadena, California

www.nasa.gov

Poster No. EA-16